DEPARTMENT OF PHYSICS
UNIVERSITY OF JYVÄSKYLÄ
RESEARCH REPORT No. 8/2011

FORCE MEASUREMENTS AND TIP SHAPE APPROXIMATION WITH THE ATOMIC FORCE MICROSCOPE

BY
JARKKO LIEVONEN

Academic Dissertation
for the Degree of
Doctor of Philosophy

To be presented, by permission of the
Faculty of Mathematics and Science
of the University of Jyväskylä,
for public examination in Auditorium KEM-1 of the
University of Jyväskylä on December 15, 2011
at 12 o'clock

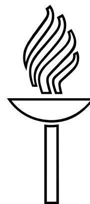

Jyväskylä, Finland
December 2011

Preface

The work reviewed in this thesis has been carried out during the years 2005-2011 at the Nanoscience Center, Department of Physics in the University of Jyväskylä.

First of all, I would like to thank my supervisor Professor Markus Ahlskog for guidance throughout the work. I also want to thank all the members of our research group and the laboratory engineers for their help.

Financial support from the Finnish Cultural Foundation and the Graduate school of Materials Physics are gratefully acknowledged.

I wish to thank my family and parents for their support.

Jyväskylä, November 2011

Jarkko Lievonen

Abstract

Lievonen, Jarkko
Force measurements and tip shape approximation with the atomic force microscope
Jyväskylä: University of Jyväskylä, 2011, 124 p.
(Research report/Department of Physics, University of Jyväskylä,
ISSN 0075-465X)
ISBN 978-951-39-4543-5 (nid.)
ISBN 978-951-39-4544-2 (verkkoj.)
diss.

The Atomic Force Microscope (AFM) is an instrument with huge impact on modern research in the nanosciences and in nanotechnology. In AFM, a tip which is sharp on a scale of nanometers or tens of nanometers, is scanning along the surface which is imaged. A few among the large numbers of factors that potentially affect the interaction between the tip and the surface were studied in the experimental work that form this Thesis. Friction and elasticity measurements with AFM and the approximation of the tip shape are discussed. Also the contribution of the imaging environment is studied.

A commercial AFM was modified into a so called environmental-AFM (env-AFM) , where the imaging conditions, such as pressure and humidity, can be controlled. The modification was done so that a minimal intrusion to the original AFM was made. The original setup of the AFM can be easily restored.

The elasticity of multiwalled carbon nanotubes (MWCNT) was measured by studying the bending due to the van der Waals force of nanotubes that were placed on microfabricated structures on silicon surfaces. The measurements were in agreement with the theoretical model that takes into account the competition between the van der Waals force between carbon nanotube (CNT) and surface and the restoring elastic force of the nanotube.

Lateral force (LF) and pull-off distance measurements as a function of humidity on a hydrophilic silicon showed a maximum at the relative humidity (RH) slightly above 30 %. The coincidence of the maximum for both measurements was shown for the first time in this work.

The precise shape of the AFM tip was determined with MWCNTs and micro fabricated steps for different kind of tips in contact and in tapping mode.

Keywords Atomic force microscopy, lateral force microscopy, friction, capillary force, carbon nanotube, elasticity, convolution

Author's address Jarkko Lievonen
Nanoscience Center
Department of Physics
University of Jyväskylä
Jyväskylä
Finland

Supervisor Professor Markus Ahlskog
Nanoscience Center
Department of Physics
University of Jyväskylä
Jyväskylä
Finland

Reviewers Professor Janne Ruokolainen
Department of Applied Physics
Aalto University School of Science and Technology
FI-00076 AALTO
Finland

Professor Marina Ruths
Department of Chemistry
University of Massachusetts, Lowell
Olney Science Center
1 University Avenue
Lowell, MA 01854

Opponent Professor Jouko Peltonen
Åbo Akademi University
Fysikalisk kemi
Porthansgatan 3-5
20500 ÅBO
FINLAND

List of Abbreviations

AFM	atomic force microscopy
APD	amplitude-phase-distance
ATR-IR	attenuated total reflection-infrared
CCVD	catalytic chemical vapor deposition
CNT	carbon nanotube
CVD	chemical vapor deposition
DLC	diamond-like carbon
env-AFM	environmental atomic force microscope
FFM	friction force microscopy
FZ-curve	force-distance curve
H_2O_2	hydrogen peroxide
H_2S0_4	sulfuric acid
HF	hydrofluoric acid
HMDS	hexamethyldisilazan
HSS	high speed steel
IC	intermittent-contact
LF	lateral force
LFM	lateral force microscopy
MFM	magnetic force microscopy
MoS_2-Ti	molybdenum disulfide titanium

MWCNT	multiwalled carbon nanotube
OTS	octadecyltrichlorosilane
PECVD	plasma-enhanced chemical-vapor deposition
PSPD	position sensitive photodetector
RH	relative humidity
SEM	scanning electron microscope
SFM	scanning force microscopy
SKPM	scanning Kelvin probe microscopy
sp	setpoint
SPM	scanning probe microscopy
STM	scanning tunneling microscopy
SWCNT	single wall carbon nanotube
TEM	transmission electron microscope
TMS	trimethylsilyl
TSB	tip set back
UHV	ultra high vacuum
XRD	x-ray diffraction

List of Publications

The main results of this thesis have been reported in the following articles:

A.I WALKEAJARVI T., LIEVONEN J., AHLSKOG M., ASTROM J., KOSHIO A., YUDASAKA M., IIJIMA S. , *Bending of multiwalled carbon nanotubes over gold lines*. Journal of Applied Physics **98** (10) (2005) 104301.

A.II LIEVONEN J., RANTTILA K., AHLSKOG M., *Environmental chamber for an atomic force microscope*. Review of Scientific Instruments **78** (4) (2007) 043703.

A.III LIEVONEN J., AHLSKOG M., *Lateral Force Microscopy of Multiwalled Carbon Nanotubes*. Ultramicroscopy **109** (7) (2009) 825.

A.IV J.T. LIEVONEN, T. PARVIAINEN, J. ASTROM, M. AHLSKOG, *AFM Tip Shape estimation Using Carbon Nanotubes and Microfabricated Steps*. Ultramicroscopy, under review..

Author's contribution

The author of this thesis has done partly the sample fabrication and the AFM measurements of publication A.I.

In A.II, the author did the assembly of the chamber, all the measurements, and wrote the draft version of the publication.

In A.III, the author did all the AFM measurements and wrote the draft version of the publication.

In A.IV the author fabricated the CNT samples, did most of the AFM measurements, most of the tip shape approximation calculations and wrote the draft version of the publication.

Other works to which the author has contributed

1) P. Koppinen, J. Lievonen, M. Ahlskog, and I. Maasilta, "Tunnel junction based displacement sensing for nanoelectromechanical systems", Journal of Physics: Con-

ference Series 92, 012051 (2007).

2) D. Mtsuko, A. Avnon, J. Lievonen, M. Ahlskog, and R. Menon, "Electrochemical deposition of polypyrrole nanolayers on discontinuous ultrathin gold films", Nanotechnology 19, 125304 (2008).

3) P. J. Koppinen, J. T. Lievonen, M. Ahlskog, and I. J. Maasilta, "Strain sensing with sub-micron sized Al-AlOx-Al tunnel junctions", Review of Scientific Instruments 81, 023901 (2010).

Contents

Preface **1**

Abstract **3**

List of Publications **9**

1 Introduction **13**

2 Atomic force microscopy **15**
2.1 Operation modes in AFM 15
2.1.1 Contact and Tapping modes 15
2.1.2 Lateral force microscopy 16
2.1.3 Force distance measurements 17
2.2 Calibration 18
2.2.1 Scanner 19
2.2.2 Cantilever: Normal force 19
2.2.3 Cantilever: Lateral force 22
2.3 Tip fabrication 24

3 Control of the AFM imaging environment **27**
3.1 The effect of the environment 27
3.2 The environmental AFM 28
3.3 Experimental 30
3.4 Environment control in commercial AFM's 30

4 Elasticity of Carbon nanotubes on surface structures **33**
4.1 Carbon nanotube basics 33
4.2 Mechanical properties of CNT's 34
4.3 Elasticity measurements of the carbon nanotubes 36
4.3.1 The Van der Waals force between the CNT and the sample . . 37
4.3.2 Elastic force of the CNT 38
4.3.3 Sample fabrication 38
4.3.4 AFM measurements 38

5 Lateral force measurements **41**
5.1 Friction and nanotribology 41
5.2 Low friction materials 44
5.3 Experimental 44
5.4 Friction on silicon and MoS_2-Ti 46
5.5 Lateral force across CNT 46

6 Humidity dependence in atomic force microscopy **53**
6.1 Laplace theory of capillarity 53
6.2 The capillary force in AFM 56
6.2.1 Effect of various parameters 56
6.2.2 Capillary effects on tapping mode 57
6.2.3 Reported capillary effects in hydrophilic materials 57
6.2.4 Reported capillary effects in hydrophobic materials 58
6.2.5 Reported capillary effects in MoS_2 60
6.2.6 Summary of previous work on the capillary force in AFM and our contribution 61
6.3 Experimental 62
6.4 Measurements 63

7 AFM tip shape estimation **67**
7.1 Convolution 67
7.1.1 Experimental 69
7.1.2 Tip shape estimation with microfabricated steps 70
7.1.3 Tip shape estimation with carbon nanotubes 70

8 Conclusions **75**

Appendixes **85**

Chapter 1

Introduction

Scanning probe microscopy (SPM) can be divided into two main fields: scanning tunneling microscopy (STM) and atomic force microscopy (a.k.a. scanning force microscopy, SFM). STM was invented in the year 1981 by Binnig and Rohrer [9]. It used a tunneling current between the sharp tip and the sample as a feedback signal. With this equipment they were able to see individual atoms on a silicon surface. Despite the high imaging capability, the STM has one drawback, which is that the sample must be electrically conductive. This limitation was overcome in 1986, when Binnig, Quate and Gerber invented the AFM [8]. In AFM, the tip is attached to a flexible cantilever. The interaction between the tip and the surface causes the cantilever to bend, which gives (usually optically) a measurable signal that acts as the feedback.

The AFM is a powerful tool for both imaging and force measurements with high precision and in very varied conditions. This thesis discusses experimental work on how to improve the understanding of AFM operation in certain of these conditions. Major topics to be discussed include experiments on how lateral forces arise in the tip-surface interaction, the effect of humidity via capillary forces, and the estimation of tip shape.

In addition to basic imaging, AFM can also be used for different kind of force measurements, including e.g. friction, adhesion force, and elasticity measurements. Measuring friction implies measuring lateral forces encountered by the tip. The carbon nanotube has a well specified circular surface that provides a testbed for investigating how those lateral forces arise as the tip sweeps over the nanotube.

Occasionally the imaging environment of the AFM must be controlled for precise interpretation of the imaging results. Critical parameters are e.g. humidity, air pressure and temperature. Humidity affects the AFM imaging both in tapping and in contact mode via the formation of capillary water bridges between the sample and the surface. In tapping mode it increases the interaction force between the tip and the sample, which can be seen e.g. in the increase of the phase shift or in the instability of the imaging. In contact mode the humidity affects the tip-sample force and the effect can be seen e.g. in the friction measurements.

Tip imaging can be done with subnanometer resolution in the height direction.

Lateral accuracy is limited by the finite shape of the tip. The distortion of the AFM images due to the tip shape is called convolution and various methods exists to reduce or to accommodate this effect. One way is to use different kinds of characterizers, which have dimensions smaller than the tip. In the method the characterizer is used to image the shape of the tip rather than the tip imaging the sample. From this image the shape of the tip is gained and can be computationally removed from the other images. A problem is that the tip tends to wear off constantly, especially during contact mode imaging, so the characterization must be done often enough. One promising object for tip shape approximation is the carbon nanotube, because of its small size, high aspect ratio (= length/diameter) and perfect cylindrical shape. By using the carbon nanotube, the approximation can be done with a high precision due to its small diameter. The drawback of the small size is that the tip shape can be approximated only by a distance corresponding to the diameter of the nanotube. This distance is typically ten nanometers or less with multiwalled nanotubes. Beyond this scale larger objects must be used. One possible solution is to use microfabricated steps. The total shape of the tip can then be obtained by combining the data from these two.

Chapter 2

Atomic force microscopy

Imaging in the AFM is done by raster scanning the tip on a sample surface. A schematic image of the AFM hardware is given in figure 2.1. The scanning motion is produced by a piezo scanner, which moves either the tip or the sample with a constant speed. In figure 2.1 the sample is moved with a PZT scanner (piezo usually made of PZT, or lead zirconate titanate, a ceramic alloy). The deflection (contact mode) or the amplitude of the oscillation (tapping mode) of the cantilever is kept constant by raising and lowering the cantilever with respect to the sample. To measure the deflection or the amplitude, a laser light is reflected from the back of the cantilever to the position sensitive photodetector (PSPD) . This signal is fed into a feedback loop. In the loop the signal, that is, the measured deflection/amplitude is compared to the setpoint value and the difference between these values is corrected by moving with the scanner the cantilever in the vertical direction. The setpoint thus determines the deflection or the oscillation amplitude of the cantilever. The amount of scanner movement in vertical direction is then presented as the topography of the sample. In AFM there are three imaging modes for sample topography: contact, tapping (a.k.a. intermittent-contact, IC) and non-contact mode. In addition to these, there are several non-topographic modes, such as force spectroscopy, nanoindentation, lateral force microscopy (LFM) , magnetic force microscopy (MFM) , scanning Kelvin probe microscopy (SKPM) etc.

2.1 Operation modes in AFM

2.1.1 Contact and Tapping modes

The contact mode is conceptually the simplest imaging mode in AFM. Here the deflection of the cantilever is kept constant during imaging. Usually a low scanning force (determined by the setpoint) is used to minimize the force during imaging, so that the wear of the tip or the sample is as low as possible. Due to the lateral forces during imaging, e.g. soft biological samples can be damaged or removed by

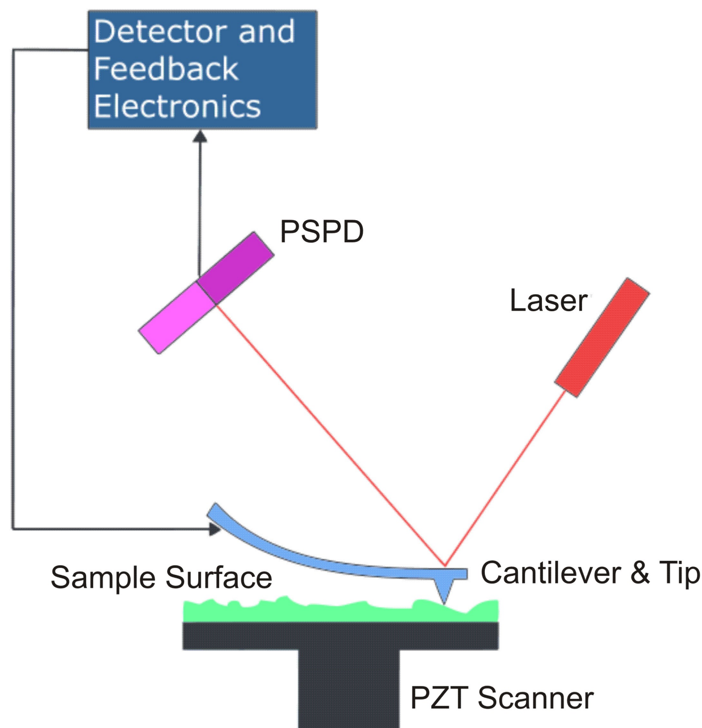

FIGURE 2.1 Scheme of the essential components of a typical AFM instrument.

the AFM tip.

In tapping mode the imaging is done by oscillating the cantilever with an amplitude ranging from a few up to a hundred nanometers. This amplitude is measured and used as a feedback signal. There are two main reasons for why the tapping mode has become the most widely used imaging mode in AFM. Firstly, all the lateral forces are almost eliminated during imaging and secondly, the imaging is more stable in ambient conditions than with the non-contact mode. The reason for the stability is that the amplitude of the oscillation is so high that the tip goes through the contamination layer of the sample surface, which reduces the effect of the capillary force.

2.1.2 Lateral force microscopy

During contact mode imaging there is torsion of the cantilever. It can be due to the topography or roughness of the sample or the change of the friction between the tip and the sample. This measurement of the cantilever twist is called lateral force microscopy (LFM) or friction force microscopy (FFM) .

Lateral force measurements are usually done by collecting the friction data in both scanning directions and determining the friction as a difference between the scans. In figure 2.2 are the lateral force signals of the trace and retrace scans and the

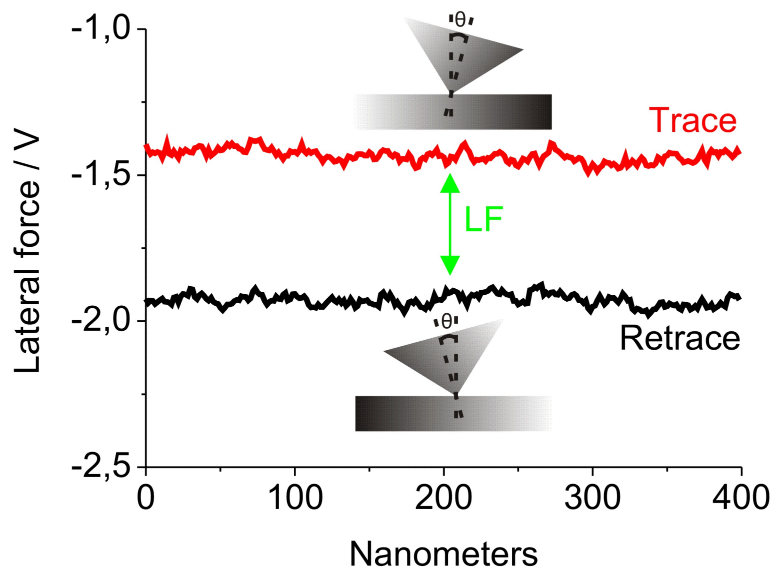

FIGURE 2.2 Lateral force is determined as the difference between the two opposite scanning directions. The figure illustrates the oppositely directed torsions of the tip.

schematic images of the corresponding tip torsions during the scan. Lateral force (LF) is measured as a difference between the two scans as indicated in figure 2.2. By this method many unwanted effects, like drift of the scanner and declination of the sample from the horizontal direction, are removed from the friction data.

2.1.3 Force distance measurements

Force measurements between the tip and the sample can be performed by varying only the height of the tip on a single point on the sample surface. Figure 2.3 represents a typical force curve (FZ-curve) , where at first the tip is not in contact with the sample (location a), so the force is constant. Then it hits the sample surface and the cantilever starts to bend (location b). The force increases linearly until the desired depth of pressing is achieved (location c). Next the tip is withdrawn upwards from the surface. During withdrawal the slope of the curve is the same as during the approach. Due to the capillary force, the tip is in contact with the sample even with negative force (locations d and e), until it snaps off as the meniscus breaks. In the approach curve a small snap-in can be seen due to the van der Waals force, which pulls the tip into contact with the sample when the gradient of the van der Waals force is greater than the restoring force of the cantilever. During retraction there is a bigger pull-off distance, due to the adhesion force A. The force can be determined from the FZ-curve as the difference between the zero-line (when the tip is not in contact with the sample) and the snap-off point, as indicated in figure 2.3. The pull-

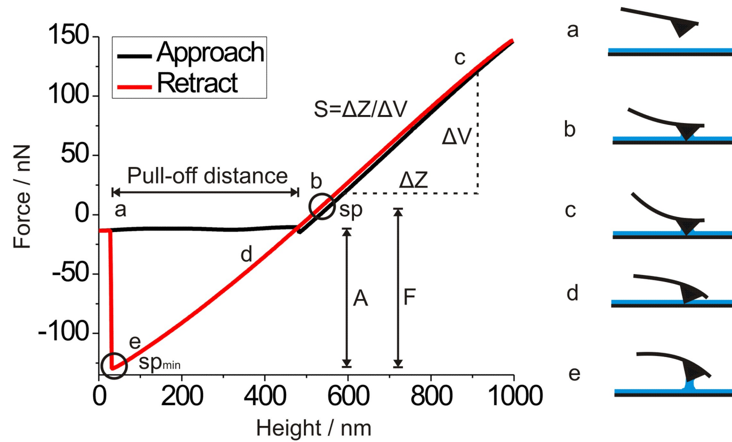

FIGURE 2.3 A typical force distance (FZ) curve. On the right, the figures labeled by letters illustrate the shape of the cantilever at the different points of the FZ-curve. A is the adhesion force and F the scanning force.

off distance and the adhesion force (figure 2.3) are related to each other through the cantilever constant k_{cl}, since

$$A = k_{cl} \cdot (pull - off\ distance) \tag{2.1}$$

Also the imaging force F (figure 2.3) can be calculated from the curve by subtracting the minimum force with which the tip is still in contact with the surface from the imaging setpoint, sp . sp is given in volts, as the reading of the PSPD is a voltage value. sp_{min}, then, is the setpoint corresponding to the minimum force. The sensitivity of the PSPD, S, is the ratio between the distance ΔZ and the detector signal in Volts ΔV. If the FZ-curve is not calibrated (force presented as volts), the imaging force can be calculated by [1]

$$F = (sp - sp_{min}) S k_{cl} \tag{2.2}$$

This is the scanning force F, given in figure 2.3.

2.2 Calibration

In order to achieve reproducible results in the AFM measurements, it's important to calibrate the instrument. The first thing is to calibrate the AFM scanner. After that the cantilever and the PSPD can be calibrated, if one wants to know the normal force during imaging. This means converting the measured volts of the PSPD into nanoNewtons. If the imaging is done in contact mode and the lateral force is collected, also that can be calibrated.

2.2.1 Scanner

The AFM scanner needs to be calibrated often enough to achieve precise results. Bruker recommends the calibration to be done in every six months. Calibration means that the voltages measured by the PSPD are converted into micrometers corresponding to the height movement of the scanner. This relationship is not linear, so a higher order fit for the conversion is required. Another aspect in addition to the nonlinearity is the hysteresis: the movement of the scanner is different when the voltage is increased compared to when it is decreased. Also cross-coupling between the three piezos (x-, y- and z-direction) occurs: movement of one piezo affects the others [1].

Calibration includes four stages. First the orthogonality of the scanning is checked. If the imaged area is not a square, it has to be corrected. Next the linearity of the piezo is corrected. The piezo has to move with a constant speed over the whole voltage range. The third and fourth stages are to calibrate the sensitivities of the XY- and Z-piezos. Usually these calibration steps are done on a calibration standard made of silicon with known dimensions. Atomic scale calibration can be done either on mica or graphite surfaces [1].

2.2.2 Cantilever: Normal force

In the following, several different methods for the calibration of the cantilever are presented.

1st method One widely used is a method by Sader et al. [53, 55]. For the calibration the dimensions of the cantilever and Young modulus of the material are required. The dimensions can easily be obtained by imaging the cantilever with an optical microscope or scanning electron microscope (SEM) . Only the thickness of the cantilever can be difficult to measure exactly. Especially because the spring constant of the cantilever is to the third power of the cantilever thickness, it has to be known with a high precision. To achieve better accuracy, the thickness is usually not measured directly, but instead the resonance frequency of the cantilever, and the thickness calculated from this frequency [41]. Once all the dimensions are known, the spring constant can be calculated from the equation

$$k = \frac{Et^3 d}{2L^3} \cos\theta \left\{ 1 + \frac{4d^3}{b^3} \left(3\cos\theta - 2 \right) \right\}^{-1}, \tag{2.3}$$

where the E is Young's modulus of the material and cantilever dimensions (b, d, L, θ, t and d) are given in figure 2.4.

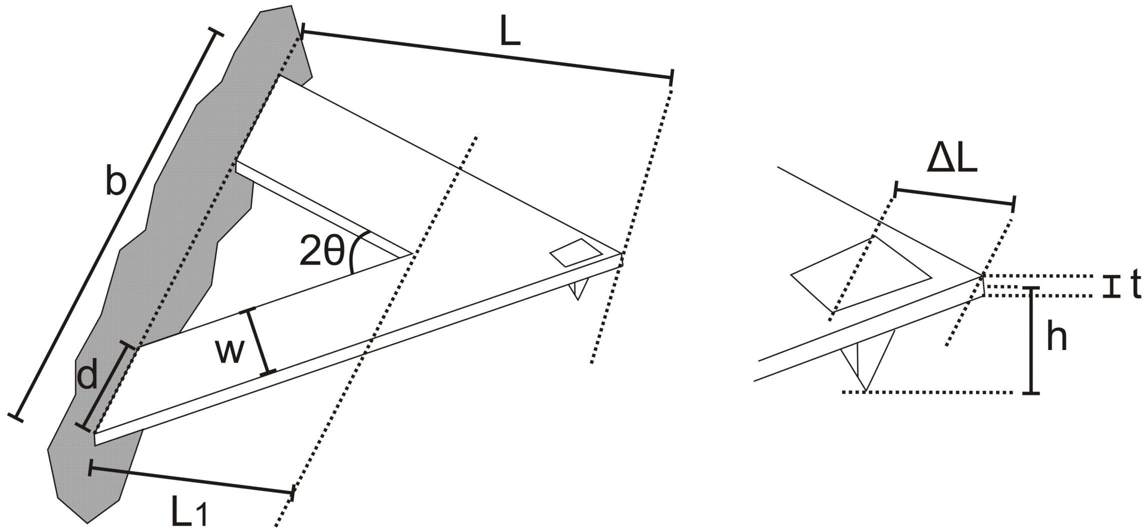

FIGURE 2.4 Dimensions of a V-shaped cantilever.

The lateral stiffness at the tip end can be calculated from the equation [43]

$$k_y = \frac{Et^3}{3(1+\vartheta)h^2}(\frac{1}{\tan\theta}\log(\frac{w}{d\sin\theta}) + \frac{L_1\cos\theta}{w} - \frac{3\sin(2\theta)}{8})^{-1}, \tag{2.4}$$

where cantilever dimensions (t, h, θ, w, d adn L_1) are given in figure 2.4. ϑ is Poisson's ratio of the material.

In the calculation of the normal spring constant of the cantilever (equation 2.3) it's assumed that the force acts at the end of the cantilever. However, usually the tip is not on the very end of the cantilever, but at some distance from the end. This distance is called tip set back (TSB) and can be several micrometers. This issue can be taken into account simply by correcting the above equation by taking the TSB into account. Ratio between cantilever with TSB $k_{\Delta L=\Delta L}$ and cantilever without it $k_{\Delta L=0}$ can be expressed as [53,55]

$$\frac{k_{\Delta L=\Delta L}}{k_{\Delta L=0}} = \left(\frac{L}{L-\Delta L}\right)^3. \tag{2.5}$$

The biggest drawback of the calibration method described above is that the thickness of the cantilever must be known with a high precision. It is usually difficult to determine especially because usually the reflectivity of the cantilever is improved by aluminum or gold coatings. The thickness of this metal layer is usually not known, but it affects the thickness of the cantilever and the spring constant of the cantilever. If the thickness is determined from the resonance frequency of the cantilever, then the effect of the surrounding air has to be taken into account since it reduces the resonance frequency.

2nd method To overcome these matters, Sader et al. [54] further developed their calibration method so that the density and the thickness of the cantilever don't need to be known. Instead the spring constant is calculated from the other dimensions of the cantilever (excluding the thickness), resonance frequency and the quality factor of the oscillations in the air. The latter two can be gained from a thermal noise spectrum. The method takes into account the change in the resonance frequency due to the surrounding air. By calculating the resonance frequency of the cantilever in vacuum from the one in air and substituting it to the equation for the cantilever spring constant, a formula for the real spring constant was obtained:

$$k = 0.1906\rho_f b^2 L Q_f \Gamma_i(\omega_f)\omega_f^2 \tag{2.6}$$

In the equation ρ_f is the density of the fluid, b and L are the width and length of the rectangular cantilever (not to be confused with the b and L of the V-shaped cantilever in the figure 2.4), Q_f the quality factor of the cantilever oscillations in the fluid (e.g. air), Γ_i the imaginary part of the hydrodynamic function and ω_f the resonance frequency of the cantilever in air. The calculation for the spring constant is not straightforward since $\Gamma_i(\omega_f)$ in the above equation includes e.g. third kind modified Bessel functions. To help the calculations Sader et al. have included to their paper a plot of the $\Gamma_i(\omega_f)$ as a function of Reynolds number

$$Re = \rho_f \omega b^2/(4\eta) \tag{2.7}$$

where η is the viscosity of the air [54].

3rd method Another calibration technique uses thermal oscillations of the cantilever. The power spectrum of the cantilever oscillations are measured as a function of the frequency using e.g. a lock-in amplifier. From this data the spring constant can be calculated, since the spring constant k is $k = k_B T/P$, where k_B is the Bolzmann constant, T is temperature and P is the area of the thermal noise power spectrum. The effect of other noise sources is eliminated by fitting a Lorentzian line to the power spectrum and then subtracting the background [29]. The Lorenz distribution in physics is used to describe forced resonances.

4th method The spring constant of the AFM cantilever can be also measured by adding a known mass to it. First the resonance frequency of the cantilever ϑ_0 is measured, then a small mass M_1 is attached to it and the frequency ϑ_1 is measured. Due to the added mass the frequency is lower. The added mass can be e.g. a tungsten sphere, which stays attached to the cantilever during the measurement, due to the

FIGURE 2.5 Misaligned tip causes mechanical cross coupling. The tip is about one micrometer off the centerline of the cantilever. The image is taken with an optical microscope.

capillary force. The spring constant k can be calculated from the equation [12]

$$k = (2\pi)^2 \frac{M_1}{(1/\vartheta_1^2 - 1/\vartheta_0^2)} \tag{2.8}$$

5th method One way to calibrate a cantilever is to use one or multiple cantilever(s) with known spring constant(s). Clifford et al. [13] used a calibrated cantilever, which they pressed with a cantilever of unknown stiffness. The cantilever was pressed on five different distances from the cantilever base. They presented also a method which uses a nanoindenter to determine the spring constant [13].

2.2.3 Cantilever: Lateral force

In order to carry out quantitative friction measurement, a calibration must be performed to convert the voltage signal on the PSPD detector, that reflect the torsion of the cantilever, into the corresponding torsional force (usually given in nanoNewtons). A calibration is also required in qualitative studies (units in volts), due to the cantilevers higher susceptibility in the normal direction than in the lateral one. The difference is typically two orders of magnitude. Also the cross coupling (a.k.a. crosstalk) affects the lateral force measurements. It can be due to an optical or mechanical origin. Optical cross coupling can be e.g. a misaligned PSPD and the mechanical one a tip that is not exactly at the center of the cantilever [37, 44], as shown in figure 2.5.

One widely used method is to scan the tip on a sloped surface and collect the lateral force signal. As the angle of the slope is known, the calibration constant can be calculated. This technique was first described by Ogletree et al. in the ref. [44]. They used an annealed $SrTiO_3$ surface as a calibration sample. After annealing the

(305) surface forms (101) and (103) planes, with known angles. Due to the sharp edge of the ridges, the sample can also be used for tip shape approximation [59]. Drawbacks in this method are the difficulties in sample fabrication and the small size of the ridges, which causes problems when calibrating blunter tips. These issues were overcome in the improved wedge calibration method (ref. [64]), which uses e.g. commercially available calibration gratings or any other sloped surface with a flat facet.

The improved wedge calibration method is based on a scan of the tip both on a sloped and on a flat surface. When the angle of the slope θ is known, the calibration constant α and the friction coefficient μ of the sample surface can be calculated. Varenberg et al. calculated equations for the α and μ from the equilibrium conditions of the forces and the force moments on a tip-surface contact point during the uphill and the downhill scans (figure 2.6 (a) and (b)). In figure 2.6 (c) is a schematic illustration of the cantilever torsion during a back and forth scan on a sloped surface. M_d is a torsion moment during downhill and M_u during uphill scan. These can be used to calculate the half-width (measured in Newton-meters)

$$W = \frac{M_u - M_d}{2} \tag{2.9}$$

and offset

$$\Delta = \frac{M_u + M_d}{2} \tag{2.10}$$

of the loop.

By assuming that for an integrated tip the length of the tip h is much bigger than the radius R ($h >> R$) and noting that on a flat surface the torsion loop offset Δ_o^{flat} must be zero, an equation for the friction coefficient of the slope can be derived. The result is

$$\sin\theta(L\cos\theta + A)\mu^2 - \frac{\Delta_o^* - \Delta_o^{flat}}{W_o}(L + A\cos\theta)\mu + L\sin\theta\cos\theta = 0. \tag{2.11}$$

So only the angle of the slope θ needs to be known about the sample. In addition the normal load L, adhesion force A, accurate torsion loop offset

$$\Delta_o = \Delta_o^* - \Delta_o^{flat} \tag{2.12}$$

and half-width W_o (measured in volts) must be determined before the calculation. Load and adhesion forces are determined from a FZ-curve as described in chapter 2.1.3. The subtraction of the equation 2.12 is done to remove the loop offset on a flat

surface Δ_o^{flat} from the one on a sloped surface Δ_o^* to gain the accurate torsion loop offset Δ_o. By this manner the effects that cause the loop offset on a flat surface Δ_o^{flat}, like signal drift, crosstalk, and misalignment of the laser on an AFM detector, are removed from the loop data.

Once we have μ from equation 2.11, the calibration factor α can be calculated from either one of the following equations:

$$\frac{\mu(L + A\cos\theta)}{\cos^2\theta - \mu^2\sin^2\theta} = \frac{W}{h + t/2} = \alpha W_o \tag{2.13}$$

or

$$\frac{\mu^2\sin\theta(L\cos\theta + A) + L\sin\theta\cos\theta}{\cos^2\theta - \mu^2\sin^2\theta} = \frac{\Delta}{h + t/2} = \alpha(\Delta_o^* - \Delta_o^{flat}) \tag{2.14}$$

Equation 2.11 gives two possible solutions for the friction coefficient μ of the slope. If one of these coefficients gives a negative calibration factor α, it's ignored, and the another mu is used to calculate the calibration constant. In the case that both μ:s implements the condition that the alpha must be positive, the correct one is determined by calculating the friction coefficient on a flat surface μ^{flat} from the two calculated α:s (equation 2.13 or 2.14) by using equation

$$\mu^{flat} = \frac{\alpha W_o^{flat}}{L + A} \tag{2.15}$$

Now there are two friction coefficients with both α:s. One on a sloped surface: μ and the other on a flat surface: μ^{flat}. These values should be almost equal, so the calibration constant that has μ:s closer to each other, is chosen to be the correct one [64].

2.3 Tip fabrication

Various methods exist for AFM probe fabrication. The fabrication hasn't changed much during the years and commercial companies use similar method as was described by Albrecht et al. in 1990 (ref. [2]). In figure 2.7 is shown the fabrication process NanoWorld Ltd., which combines anisotropic and isotropic wet etching. First a silicon wafer is oxidized and a photo resist is deposited to the back of the wafer. Photo resist is exposed through a mask, as is shown in figure 2.7 (a). Similar photolithography and development is done to the front side of the wafer. The exposed silicon oxide is wet etched from both sides of the wafer (figure 2.7 (b)). Photo resist is dissolved and the silicon is anisotropically wet etched with KOH in several steps (figure 2.7 (c)). The tip is complete when the oxide shield on top of the tip falls off. Silicon oxide is removed by isotropic wet etching. To protect the tip side of the probe during anisotropic wet etching, a silicon nitride layer is deposited on

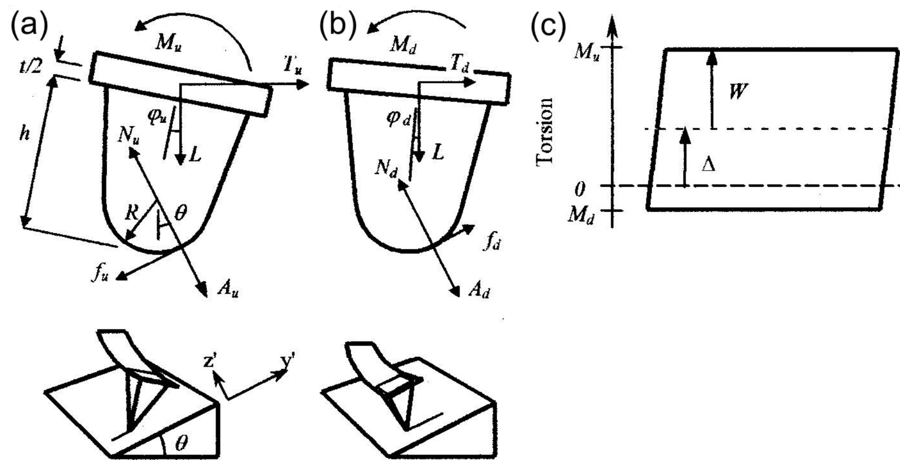

FIGURE 2.6 Forces acting on the AFM tip during (a) uphill and (b) downhill motion. (c) Torsion of the cantilever on a back and forth scan on a sloped surface. W is the half-width and Δ the offset of the loop [64].

the wafer (figure 2.7 (d)). The back side of the wafer is etched with KOH to gain the desired thickness of the cantilever. Finally the silicon nitride is removed with an isotropic wet etch and the tip fabrication is complete (figure 2.7 (e)).

In the work by Albrecht et al. various methods for the tip fabrication were studied. Tip radiuses were in most cases less than 50 nm [2]. Burt et al. developed a method which uses a triangular SiO_2 etch mask, which converges the etching planes into a single point. By this method they were able to fabricate tips with typical radius of less than five nanometers and less than two nanometers after oxidation sharpening [10]. Sharpness can be further enhanced by oxidation, to produce ultra sharp tips. This method takes advantage of the irregular oxidation of the tip end, since the highly curved tip end tends to oxidize more than the flat edges of the probe. Thus the sharpness of the tip increases. After oxidation, the oxide layer is removed for example with HF to passivate the tip against further oxidation. The final result is a silicon tip with a sharp silicon oxide end (the radius can be less than a nanometer) [38,48]. Further progress in the fabrication processes has led to the development of nanoneedles, with length of several micrometers, a sharp end and high aspect ratio (side angle only a few degrees) [71]. Nanoneedles can be prepared by etching [71] or by CVD method [26]. Some measurements for example about dynamics of the water meniscus has been done with these needles [31] but a wider use in atomic force microscopy is yet to come [71].

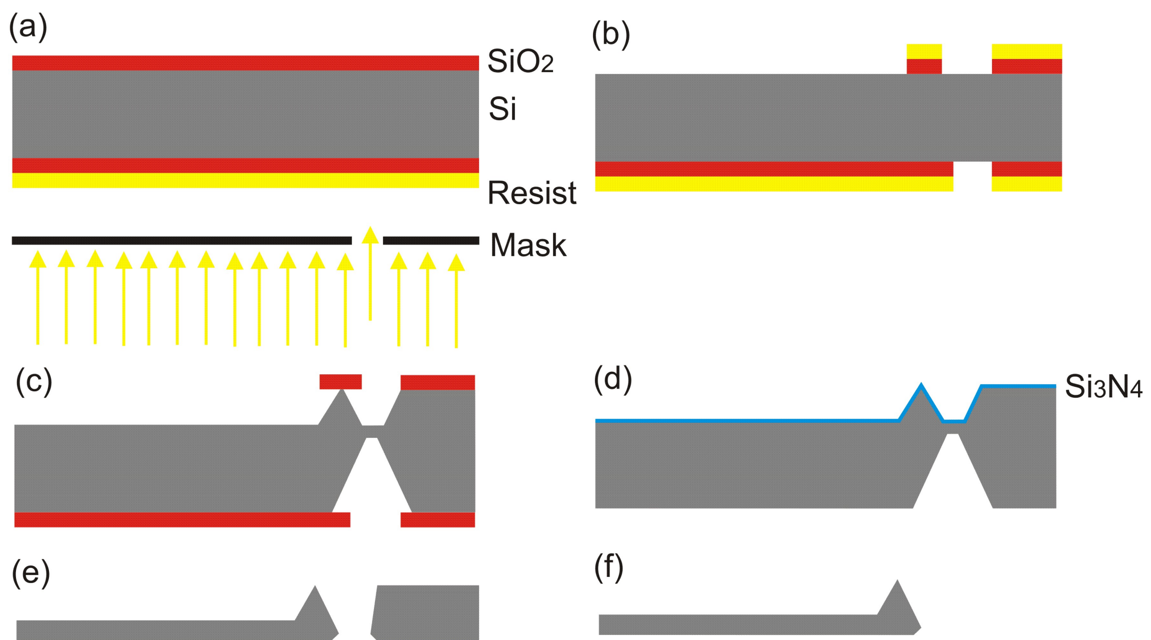

FIGURE 2.7 (a) Resist is exposed through a mask. (b) Silicon wafer after photolithography and wet etch of the silicon oxide. (c) Photo resist is removed and the silicon etched with the KOH. (d) SiO_2 removed and the Si_3N4 deposited to protect the front side of the probe during etching. (e) Probe fabrication is finished after the removal of the silicon nitride.

Chapter 3

Control of the AFM imaging environment

Imaging conditions such as humidity and pressure can significantly affect the AFM imaging in both contact and tapping mode. For that reason it's important to be able to control the imaging conditions to gain for example repeatable friction or phase shift measurements.

- A chamber was constructed and a commercial AFM instrument placed inside, which allowed the AFM to be operated in a controlled atmosphere. This instrument was used for the work in chapter 6 on the humidity dependence of AFM operation. [Publication A.II].

3.1 The effect of the environment

The amount of water on a sample surface depends on the humidity conditions of the surrounding air. The structure and amount of water on a hydrophilic silicon oxide surface at room temperature has been studied with attenuated total reflection-infrared (ATR-IR) spectroscopy . Relative humidity (RH) was varied from zero to hundred percent and the corresponding water thickness determined. Two kinds of phases of water were observed: ice like and liquid water. The first monolayer of water formed with RH of 10 % and increased up to ten monolayers with 100 % relative humidity [3].

The environment of the AFM can give significant contribution to the images. One example of this is a phase shift of the drive signal and the signal collected from the detector during tapping mode imaging. The thickness of the water layer influences the time for the tip to escape from the sample surface. The increasing time also enhances the phase shift. Incorporating the phase shift to the humidity conditions is not straightforward since many other factors can also increase the phase shift. Such

as for example topography of the sample (boundaries increases the phase shift) and hardness of the sample (soft areas damps the oscillation of the cantilever) [57].

In ambient conditions there is usually a contamination layer (mixture of water and hydrocarbons) on the sample surface. This layer affects the non-contact mode imaging, since the tip-sample interaction is affected by the capillary force between the probe and the contamination layer. Imaging can be done either above or inside the contamination layer. The first one usually gives low resolution and the latter is difficult to perform so that the tip doesn't jump into contact with the sample. Non-contact mode for biological samples in liquid has also been done. Still the true atomic resolution in non-contact mode requires UHV (ultra high vacuum) conditions [15].

Another example of humidity dependence can be found in friction measurements, which typically shows a maximum at RH = 30 %. The reasons for this trend are yet not fully clear, but different kinds of explanation are given by numerous research groups. This issue will be discussed in chapter 6.2.3.

3.2 The environmental AFM

It is sometimes useful in AFM imaging to control the imaging condition, such as humidity and pressure. For this purpose a commercial AFM was placed inside an aluminum chamber. Small modifications to the AFM were done e.g. to reduce the vacuum pumping time and to improve the optical vision to the sample surface.

The XE-100 AFM from Park Systems (former PSIA corp.) was chosen for the project especially because it could be easily separated into two distinct parts, as is shown in figure 3.1. The frame part includes optics and an electronic board while the core part has all the central parts for AFM imaging. The core part has the micrometer screws to move the sample, separate xy- and z-scanners, laser diode, laser spot alignment mirror and the position sensitive photo detector (PSPD). The frame part was placed outside the environmental chamber to reduce the vacuum pumping time and to extend the range of operating conditions (pressure and humidity) that can be applied.

The core part of the AFM was put inside the custom made aluminum chamber (figure 3.2 (a)). It was desirable to be able to control the laser, mirror and the sample location from outside of the sample. To achieve this, four retractable staves were put through the chamber walls for laser diode and mirror control. Staves for the laser diode can be seen on the top of the chamber and staves for the mirror to the left of the chamber in the figure 3.2 (c). The placement of the sample can be controlled with two electric motors that have encoders outside the chamber. The vision to the AFM cantilever and to the sample surface had to be improved by placing an extra lens near the z-scanner (figure 3.2 (b) and (c)) and a long range microscope together with a CCD camera on top of the chamber.

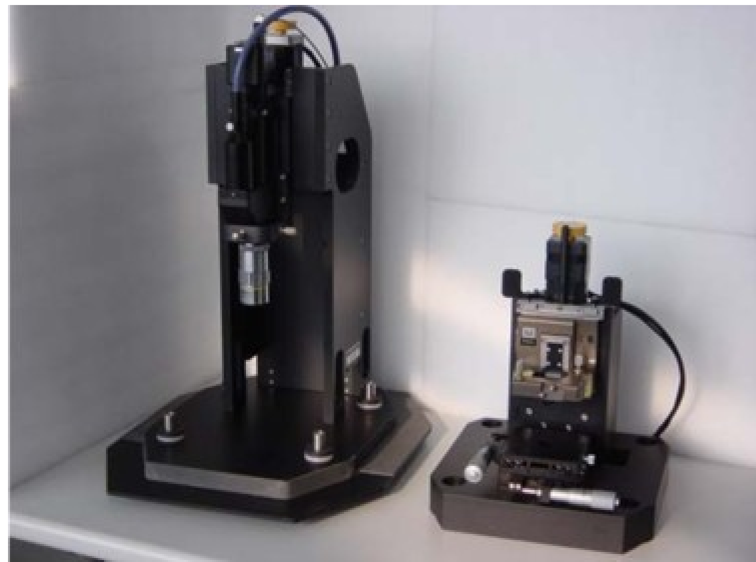

FIGURE 3.1 XE-100 AFM from the Park Systems. The AFM is separated into two parts: the frame part on the left and the core part on the right.

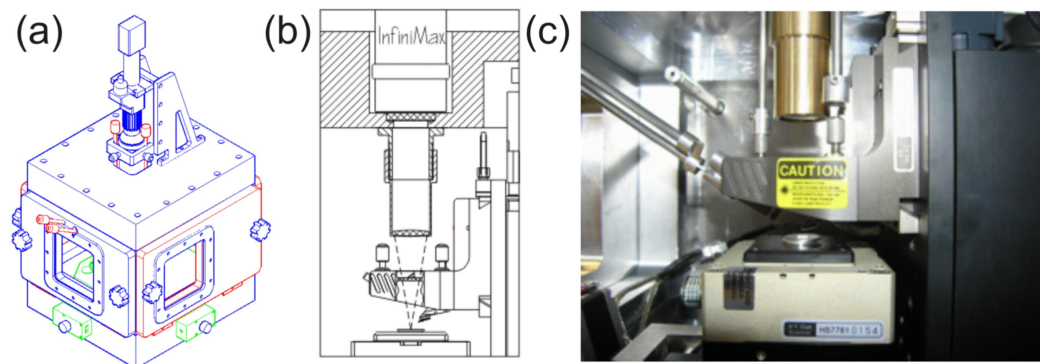

FIGURE 3.2 (a) Schematic illustration of the environmental chamber. (b) Drawing of the scanner and the added extra lens. (c) Picture from the inside of the chamber. Adjustment staves for the laser are on the left and the pressure/temperature sensor on the upper left corner.

The environmental AFM has two pumps: a dry scroll vacuum pump and a turbo pump fixed to the back of the chamber. The pressure is measured with Penning and Pirani gauges. The humidity inside the chamber can be increased by introducing water vapor into the chamber. It's done by heating a small amount of water (about 1 ml) inside the chamber with a thermal resistor. Humidity can be decreased with drying silica pellets which absorb water from the air. Pellets are placed inside a plastic tube that has a small fan in one end. The fan takes humid air from the bottom of the chamber and pushes it through the layer of drying pellets into the top of the chamber. Also different kind of non-corrosive gases (e.g. nitrogen or helium) can be brought to the chamber from the valve on the left side of the chamber. The chamber doesn't allow exact control for the humidity and the temperature is the ambient one. Still, those can be measured with high precision with the Vaisala Humicap HMT337 humidity/temperature sensor.

3.3 Experimental

The surrounding air dampens the oscillations of the cantilever during imaging. It can thus affect the imaging because higher driving force is required for the cantilever compared to the vacuum conditions and because of the decreased Q-factor. The spectrum of the cantilever vibrations were measured both in normal air pressure and in a 10^{-4} mbar pressure. In both cases the first three resonance peaks were observed for a soft cantilever with spring constant of 0.6 N/m and the first resonance frequency at 51 kHz. Data is shown in figure 3.3. The height of the first resonance peak increased approximately one order of magnitude, but other resonances weren't affected.

To test the performance and the noise levels of the AFM an atomic step was imaged in air with a closed chamber. The imaged sample was a freshly cleaved graphite step. Figure 3.4 shows the topography signal across the atomic step. The height of the step is about three Ångströms. Noise is filtered out from the image. Thus the system performs adequately despite the major reengineering of it.

Also preliminary measurements of the adhesion force in humid conditions on a silicon oxide surface were performed. Figure 3.5 shows a typical FZ-curve with a RH of 64 %. The pull-off distance is indicated with dotted lines and was above 150 nm. The pull-off force was estimated to be about 85 nN. Such measurements are described in section 6.4 for a large range of humidities.

3.4 Environment control in commercial AFM's

In recent years many commercial environmental AFMs have come to the market. One of them is the environmental chamber announced by Agilent Technologies in

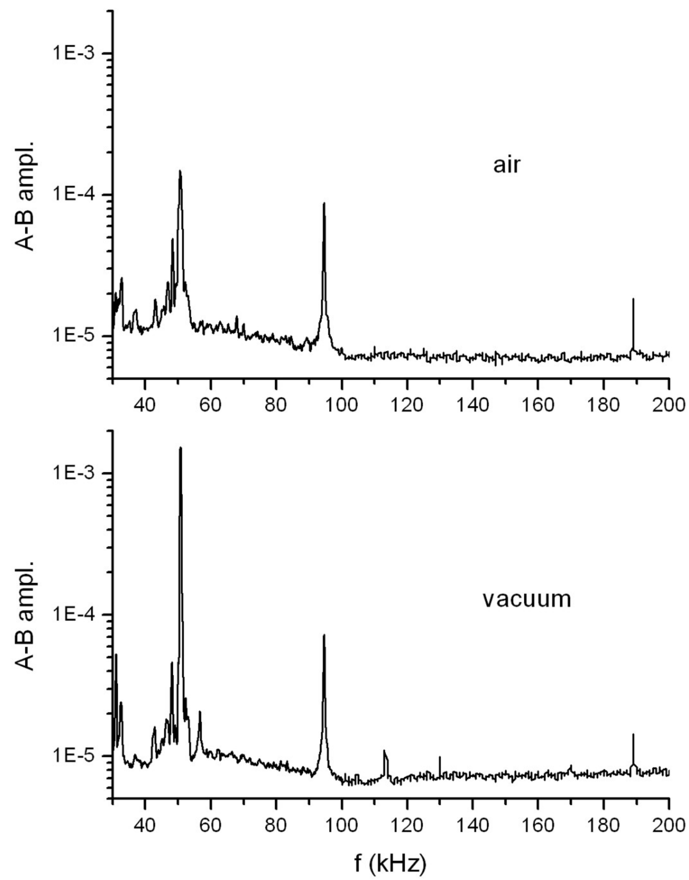

FIGURE 3.3 Deflection of the cantilever (A-B signal) measured with a spectrum analyzer both in a normal air and in a vacuum.

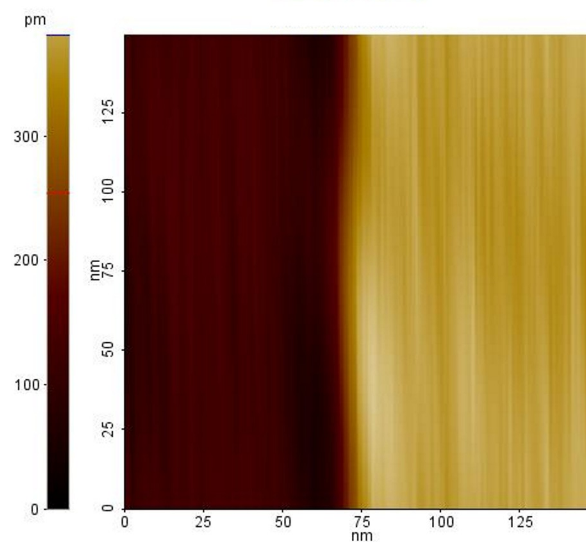

FIGURE 3.4 Atomic step on a graphite imaged with the AFM.

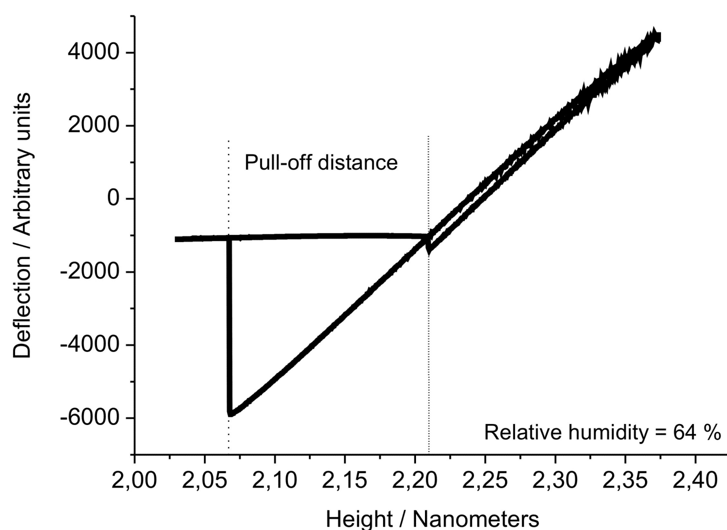

FIGURE 3.5 Force-distance (FZ) curve on a SiO_2 surface. Z is the distance the piezo-element moves the tip vertically above the surface. On the Y-axis is shown the deflection of the cantilever as measured by the PSPD. The arrows indicate direction of the movement. The hysteretic behavior between the dashed lines show the extent of the pull-off distance upon retraction.

2006. Inside the chamber humidity and oxygen levels can be measured and controlled. Also different kind of gases and liquids can be introduced to the chamber. Park Systems released in 2008 a cell chamber designed especially for improving the life expectance of living cells. In the chamber temperature, humidity and pH can be controlled. Bruker has integrated an AFM with a glove box to control the imaging conditions (announced in the year 2011).

Chapter 4

Elasticity of Carbon nanotubes on surface structures

The single wall carbon nanotube (SWCNT) is a cylinder of a single layer of graphite (that is, graphene) with typical diameter of less than two nanometers. Two or more cylinders within each other, are called multiwalled carbon nanotubes (MWCNT) [56]. Nanotubes were first found by Sumio Iijima (though there were some previous work) in the year 1991 by using a transmission electron microscope (TEM) [30].

● In this chapter we describe a simple method to measure with the AFM the elasticity of CNT's on surfaces with microfabricated structures. [Publication A.I].

4.1 Carbon nanotube basics

The three main methods to fabricate carbon nanotubes are laser vaporization, arc synthesis and vapor growth [56]. In the laser vaporization method a metal-graphite composite target is put into a high temperature oven and a laser spot is focused onto it. Then the produced soot is swept from the target to a cooled collector by a flowing gas (e.g. Argon) and carbon nanotubes are collected from there [24]. Carbon arc synthesis uses two carbon rods close to each other. There is a voltage of about 20 V and 100 A current between the rods and they are surrounded by some gas (e.g. helium) to cool down the process. During the synthesis the nanotubes form at the negative electrode (cathode) [56]. In the vapor growth method (a.k.a chemical vapor deposition (CVD) method) nanotubes are grown from catalytic metal particles exposed to hydrocarbon gases at elevated temperatures [16].

The carbon nanotube is a cylinder formed from carbon atoms with high aspect ratio (= length/diameter). Nanotubes are classified by the chiral vector C_h, which is perpendicular to the axis of the nanotube. Nanotubes can also be classified according to the symmetry. If the CNT's mirror image has identical structure compared to the original one, it's an achiral nanotube. There are two two cases of achiral nano-

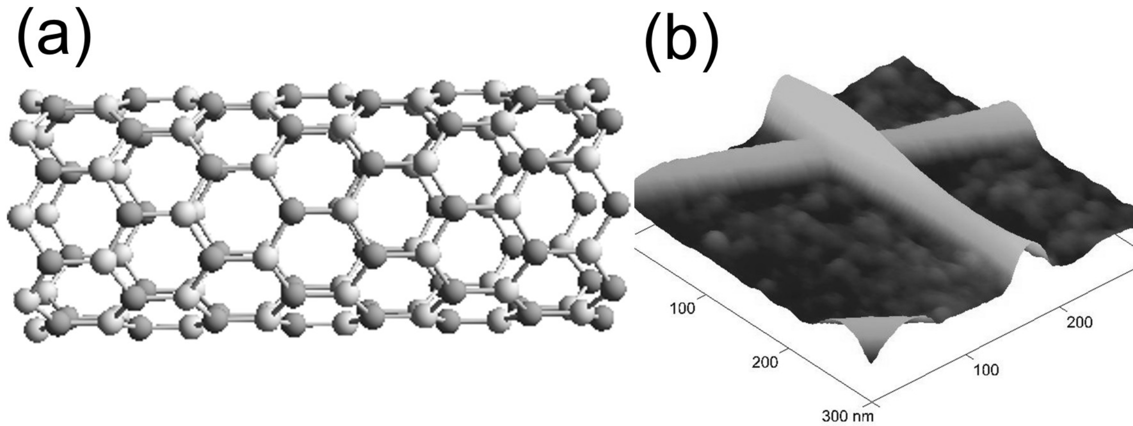

FIGURE 4.1 (a) Zigzag carbon nanotube. (b) Two crossing nanotubes imaged with an AFM. Image size is 300 nm, diameters of the nanotubes are 8 nm (lower) and 6 nm (upper).

tubes, armchair ($C_h = (n, n)$) and zigzag ($C_h = (n, 0)$) CNT's. In the figure 4.1 is an image of a zigzag nanotube. The mirror image of other nanotubes is not identical with the original one, and are called chiral nanotubes [56].

Carbon nanotubes can be either metallic or semiconductive depending on the chirality and the diameter. It can be shown that the nanotube ($C_h = (n, m)$) is metallic, if the subtraction (n-m) is a multiple of three. Especially armchair nanotubes, which have $C_h = (n, n)$, are always metallic, 1/3 of zigzag CNT's are metallic, and the rest of them semiconductive [56].

4.2 Mechanical properties of CNT's

One of the notable properties of nanotubes is their high stiffness. Many studies have measured values for CNT's Young's modulus E to be one teraPascal or even more in the axial direction. In the radial direction the Young modulus is typically one or two orders of magnitude lower.

Wong et al. determined an average value of $E = 1.28 \pm 0.59$ TPa in axial direction. They didn't observe any dependence of the Young's modulus on the diameter of the CNT's. Measurements were done by spinning nanotubes on a low friction MoS_2 surface and fixing the one end with SiO pads. Then the nanotube was bent horizontally with an AFM tip and E calculated from the collected bending and force data [69].

Nanotubes are also very flexible and can be bent into high angles without breaking them. Falvo et al. used an AFM to distort a nanotube into different shapes. They concluded that CNT's withstand a local strain $\epsilon = r_0/r_c$ of as high as 16 %. In the equation r_0 is the radius of the CNT and r_c, the radius of the nanotube curvature. The strain was estimated from a measurement where they bent a 6.8 nm diameter

nanotube to a curve with a radius of about 40 nm [17].

Yu et al. studied the strength of the MWCNTs up to the breaking point with an AFM. The nanotube was attached between two AFM tips with a carbonaceous material. Firstly, the residual organic material inside the SEM chamber is dissociated (split into smaller particles) with the electron beam and deposited on the MWCNT/tip interface. Next the organic contaminants migrate to the location of the focused electron beam, dissociate and deposit on the contact point. By this method CNT's were strongly attached to the AFM tip. Nanotubes were mounted from both ends to two different AFM tips and the measurement was done by stretching the CNT until it breaks. In the measurement a strain as high as 12 % was found (change in the length of the nanotube) before the failure. The total range of maximum strains before the breakage ranged from 2 to 12 percents. Young's modulus were between 18 GPa and 68 GPa for the 19 different MWCNTs. Young's modulus determined only for the outermost layer were 270-950 GPa. Authors suggests that only the outer layer is strongly bonded to the tips, giving high E. Young's modulus for the whole MWCNT is lower due to the low van der Waals interaction between the different layers as the pulling is continued after the breakage of the outermost layer [74].

Radial elasticity of the CNT's with radiuses between 2 and 12 nanometer and a constant ratio between the inner R_{int} and the outer R_{ext} radiuses of $R_{int}/R_{ext} = 2.2 \pm 0.2$ were studied by Palaci et al.. They deposited nanotubes on a silicon surface and measured the elasticity of the CNT's using an AFM. The tip was indented to the sample covered with nanotubes while the sample was oscillating with a small amplitude of 1.3 Å. They calculated the Young's modulus E by using the Hertz model. The modulus had a sharp decrease with increasing radius of the CNT, with radiuses below four nanometers and saturated at 30 ± 10 with the R_{ext} from 4 to 12 nanometers [45].

The radial compression of the CNT's has been studied using the indentation mode of the AFM. In the method, the AFM tip is placed on top of the CNT and then the sample moved upwards. This causes both the cantilever to bend and the CNT to compress. The measurement was done with five different pressing forces between 220 and 1670 nanoNewtons. These force curves showed nonlinear behavior. In this work the Young's modulus E was defined to be $E = (h/A)(dF/dh)$, where h is the height of the CNT before the indentation and A is the area of the contact. The dF/dh is the slope of the force curve at the turning point, where the approach of the sample towards the tip ends and the retraction begins. With the two smallest indentation forces of 220 nN and 420 nN, E was about 10 GPa. The deformation of the nanotube was mainly due to the shape change of the cross section. With the higher forces (from the 420 nN to the 1670 nN) the deformation of the CNT is different, since the shells of the CNT are further compressed, which increases the stiffness of the CNT. Young's moduli with these bigger forces were much higher: about 60 GPa (850 nN force) and about 80 GPa (1200 nN and 1670 nN forces) [60].

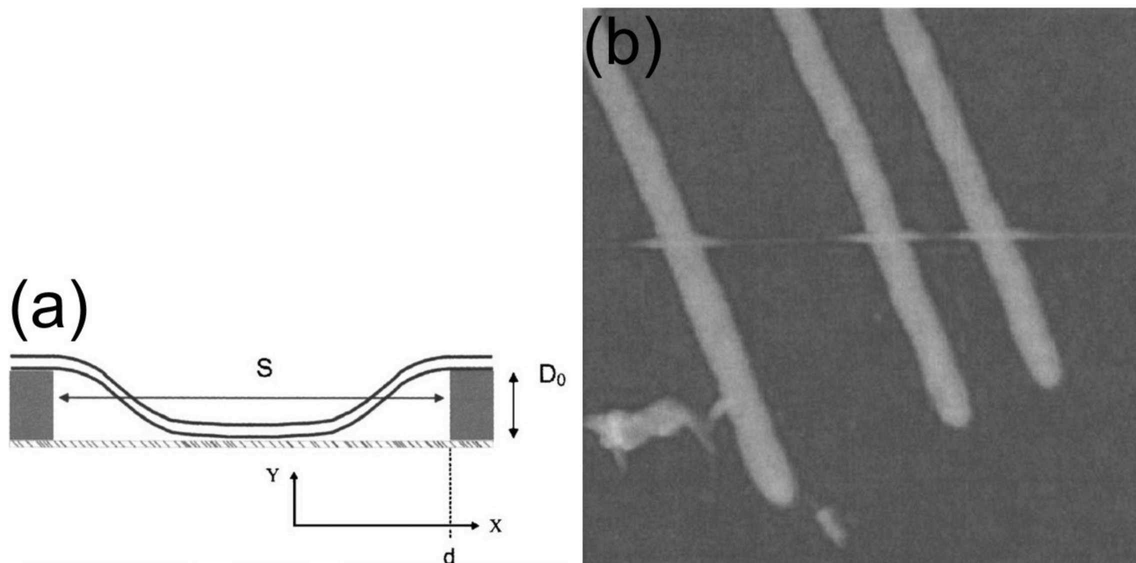

FIGURE 4.2 (a) CNT between two gold lines. (b) AFM image of a CNT crossing 32 nm high gold lines. Imaged area is $1.5 \cdot 1.5\ \mu m^2$

High reversible deformations of CNT's have been seen previously also by Yu et al., who observed up to 40 % reversible deformations of the nanotubes, when imaged with the AFM in tapping mode [73].

Hertel et al. have studied the deformation of CNT's due to the van der Waals force on a silicon surface. They did molecular mechanics calculations for different kinds of nanotubes. The deformation was shown to depend on the diameters and the shell numbers of the nanotubes. For a 6.7 Å SWCNT there wasn't any deformation, but for a 54.2 Å nanotube the deformation was as high as 42 %. The compression was reduced as the number of inner shells was increased. The reason for the deformation is the increase in the binding energy as the nanotube-sample contact area increases. MWCNT's are more rigid than SWCNT's, so the deformation requires more energy to occur and is thus smaller [27].

4.3 Elasticity measurements of the carbon nanotubes

The elastic properties of CNT's were studied in this Thesis by imaging with the AFM nanotubes that were laying on the edges of lithographically fabricated steps. The experimental setup is schematically depicted in figure 4.2 (a). The two main forces affecting the CNT are the van der Waals force, which tends to bend the CNT towards the sample and the opposing elastic force of the nanotube. The balance between these two forces determines the distance that the nanotube is suspended before it touches the sample surface. These distances were measured with three different step heights of 16, 32 and 45 nanometers and diameters of MWCNT's ranging from 3 to 13 nm.

4.3.1 The Van der Waals force between the CNT and the sample

The Van der Waals force is an electromagnetic force between permanent or induced dipoles. There are three types of van der Waals forces: orientation (Keesom), induction (Debye) and fluctuation (London) interactions. In the orientation interaction the force is between the freely rotating permanent dipoles. The induction van der Waals force is a force between a permanent dipole and an induced dipole. The fluctuation interaction arises from the polarization of a molecule due to the fluctuations in the charge distribution of a neighboring molecule. The first two interactions (orientation and induction) are always on the average attractive. The third (fluctuation) is repulsive at small separations due to the overlapping of the electron clouds of the molecules and attractive at larger distances [7].

The interaction energy of the van der Waals force is proportional to the distance by $E(r) \approx r^{-6}$, at distances less than ten nanometers. At larger distances the dependence is as r^{-7} due to the retardation effect. It's a phenomena where the dipole moment of a dipole changes during the time that it takes for an electromagnetic wave to travel from the dipole to the other dipole, to interact, and another photon to return to the first dipole [7].

Generally the van der Waals force is described by the Hamaker constant. This method assumes that the interaction energy of two bodies can be calculated by summing the pairwise interactions. By this manner, effects like screening (interaction is lowered due to the mobile charges) and the intervening medium are not taken into account. The Hamaker constant is typically $10^{-20} - 10^{-19} J$ for the interactions between the solids and the liquids across vacuum and air. In any medium, the Hamaker constant is typically an order of magnitude lower [7].

The van der Waals force between the nanotube and the sample can be calculated by assuming that it has a $E(r) \approx r^{-6}$ dependency. From the equation the vdW force between the CNT and the sample can be calculated by first integrating the previous attraction energy between a mass point and a half-space. Next the shape of the CNT is taken into account by integrating the previous expression along the nanotube. The vdW energy is then

$$dE_{vdW} = \frac{Adx}{6} \frac{R^2}{[y(y+2R)]^{3/2}} \tag{4.1}$$

In the equation 4.1 A is the Hamaker constant, R is the radius of the CNT and the distances x and y as in the figure 4.2 (a). The equation 4.1 is gained by taking into account only the attractive dipole-dipole interaction. The repulsive part, due to the Pauli principle, is not taken into account. It's assumed that the minimum CNT-sample distance is 0.4 nm.

4.3.2 Elastic force of the CNT

In the elastic force calculation it was assumed that there was no torsion of the CNT, the strain was small, and the nanotubes were clamped on the edge of the microfabricated line structures and on the point where the CNT first touches the sample surface. With these assumptions the profile $y(x)$ and the elastic energy E_{el} of the CNT are

$$y(x) = D_0[3(\frac{x}{d})^2 - 2(\frac{x}{d})^3] \tag{4.2}$$

and

$$E_{el} = \frac{\pi E R^4}{8} \int_0^d (\frac{d^2 y}{dx^2})^2 dx \tag{4.3}$$

The thickness of the line is D_0, d is the distance that the CNT is suspended and E is the Young's modulus.

4.3.3 Sample fabrication

Samples for the elasticity measurements of the CNT's were fabricated by electron beam lithography. After the patterning of the resist by the scanning electron microscope, the sample was developed and a layer of gold was evaporated to the sample surface in vacuum. Three different evaporation thicknesses D_0 were used: 16, 32 and 45 nanometers. After evaporation the resist was removed with acetone. Finally the multiwall carbon nanotubes were randomly spinned on the surface. The diameters of the CNTs were between 3 and 13 nanometers. They were fabricated in two different ways: catalyst-free plasma-enhanced chemical-vapor deposition (PECVD) [35] and the arc discharge method (MER corporation).

4.3.4 AFM measurements

Imaging of the CNTs was done in tapping mode with a Nanoscope IV AFM from Veeco (now Bruker). First a nanotube that was descending from the gold line to the silicon oxide (SiO_2) surface was searched by scanning a large area of about ten micrometers. Schematic illustration of a nanotube between two gold lines can be seen in figure 4.2 (a). Once a suitable CNT is found, the scan size is decreased and the profile taken by scanning along the nanotube (figure 4.2 (b)). From this scan the distance d, in which the CNT was not touching the sample surface was determined. The diameter of the CNT Θ was determined by scanning across the nanotube on the section where it was clearly in contact with the sample surface.

The distances, for which the CNTs were suspended, were measured with three different step heights and varying CNT diameters. Results are given in figure 4.3.

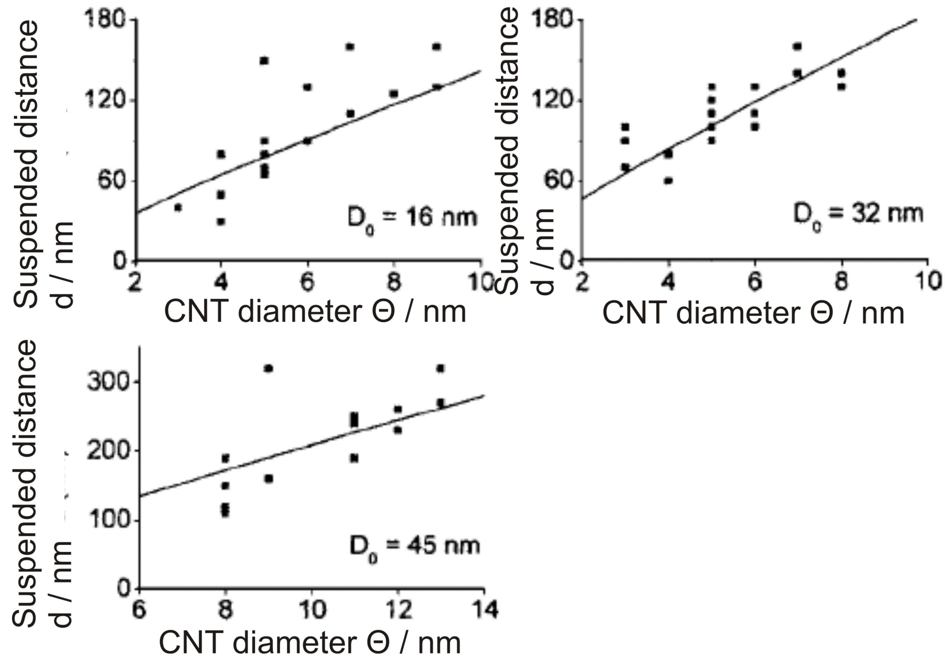

FIGURE 4.3 Measured distances (d), as a function of the CNT diameter, for which the CNTs are suspended with different step heights D_0 (see figure 4.2(a)). The solid line is a theoretical distance, based on equilibrium between van der Waals and elastic force.

The solid line is based on a theoretical model of a balance between the van der Waals force (equation 4.1) and the elastic force (equation 4.3) of the CNT. In the calculations a ratio of $Y/A = 5 \cdot 10^{29}$ was used. It's a smaller ratio than the typical values of $Y = 1\,TPa$ and $A = 1 \cdot 10^{-19}$ would give. So the value of Young's modulus may be slightly lower than one TeraPascal. Also the Hamaker constant could be higher than the assumed $1 \cdot 10^{-19}$.

There are some possible sources of error in the analysis of the measurement results. In the elastic force calculations the hollowness of the CNTs is not taken into account. For the smaller CNTs fabricated with the PECVD the inner radius is 0.4 nm [35], so the approximation is acceptable. Also the elastic energy is proportional to the fourth power of the outer radius R (equation 4.3), thus the inner radius has a minor effect on the energy term. In the theoretical calculations, it's assumed that the nanotubes deform only through bending. However the deformations of the CNTs in the measurements are so high, that also the cross section can be flattened and reduce the stiffness of the CNT. One thing is the capillary force, which is ignored by assuming that the van der Waals force is the dominant one. Due to the hydrophobicity of the nanotubes, this assumption is considered to be valid. The bending was assumed to be elastically reversible. To study the validity of the assumption, the maximum strains, which occur in the end points of the freely hanging CNT, were calculated. Most of the strains were below the five percent strain, which is widely considered to be the tensile strength of the CNT [52]. The big question is the validity of the contin-

uum elasticity theory, which especially for smaller nanotubes with diameter close to two nanometers is not justified. So for the smaller nanotubes a more sophisticated model should be adopted.

Chapter 5

Lateral force measurements

The AFM can be used to measure the friction on a nanoscale, as was discussed in the chapter 2.1.2. In this scale the frictional properties can vary significantly between different kinds of samples. One factor is the formation of a humidity induced capillary bridge between the tip and the sample, which is presented in the next chapter. In this chapter we describe friction measurements for three different materials at ambient, uncontrolled humidity: Hydrophilic and hydrophobic silicon and molybdenum disulfide titanium MoS_2-Ti , which is used as a low friction coating. In the nanoscale, the lateral forces that show up as friction do also depend on the topographical features of the surface, unless it is atomically smooth. Such lateral force was measured across a MWCNT, which provides a highly accurate known shape for investigating the topographic contribution to friction.

● Friction was measured with AFM on hydrophilic and hydrophobic silicon with different normal forces.
● Similar measurements were done also on molybdenum disulfide titanium MoS_2-Ti.
● Lateral force in contact mode was measured across MWCNT's with different tip shapes and CNT radiuses. [Publication A.III].

5.1 Friction and nanotribology

At the macroscopic level friction is usually described by a coefficient of the friction μ. It's defined as a ratio between the friction force F_μ and the normal force F_N:

$$\mu = F_\mu / F_N \tag{5.1}$$

It says that the friction is proportional to the normal load (Amonton's first law). The friction coefficient is a simple way to describe a complex phenomenon. It e.g.

assumes that the friction doesn't depend on the area of contact (Amonton's second law) or sliding velocity (Coulomb's law) [72].

There are two mechanisms behind the friction of two smooth macroscopic objects (figure 5.1 (a)): adhesion and plowing. The total friction force F_μ can be thought as a sum of these two forces [40].

The adhesion force is due to the contact between the asperities of the two materials. When the end atoms of these asperities are in near contact a force between them occurs. The force is a sum of the attractive and repulsive forces. The attractive force can be due to the metallic, ionic or van der Waals bonding. The reason for the repulsive force is the overlapping electron clouds. When the objects begin to move relative to each other, the forces between the asperities resist this movement. At first the asperities deform elastically and are preventing the movement. If the force is increased, at some point the interatomic forces between the asperities are overcome and the objects start to slide. During sliding the asperities can deform plastically. A simple way to approximate this adhesion force F_{adh} is to calculate it as a product of the real contact area A_r times the shear strength s:

$$F_{adh} = A_r s \tag{5.2}$$

The shear strength s is the shear stress needed to start and sustain the sliding. The real contact area A_r can be simply calculated as a sum of the areas of the individual asperities: $A_r = \Sigma A_i$ [40].

Plowing friction is caused by the asperities of the harder material going through the softer ones. It's approximately the area of the softer material in the direction of the movement A_0 times the pressure needed for plastic deformations to occur in the softer material. The pressure is approximately the hardness of the softer material H, so the plowing friction can be written as [40]

$$F_{plow} \approx A_0 H \tag{5.3}$$

The study of friction at nanoscales as a scientific and engineering topic is the domain of nanotribology. On a nano- and micro scale the friction comes both from the material properties of the surface and the topography (that is, roughness) of the sample. In the figure 5.1 (b) is an AFM tip, which can be regarded as a single asperity contact with the sample. The topographic effect can be seen e.g. when scanning across an asperity: On the ascending edge of the asperity, there is an extra torsion force to the tip due to the positive slope, which increases the friction signal. On the contrary, a decrease in the friction signal can be seen on the descending edge due to the negative slope. This is known as the ratchet mechanism. Besides this effect, also the simple collision of the tip to the ascending edge can enhance the friction signal. On the descending edge a small relaxation of the tip torsion can be seen, which shows as a decrease in the friction signal. The difference between, the ratchet mechanism and the collision effect, is that in the former the tip is in stable torsion

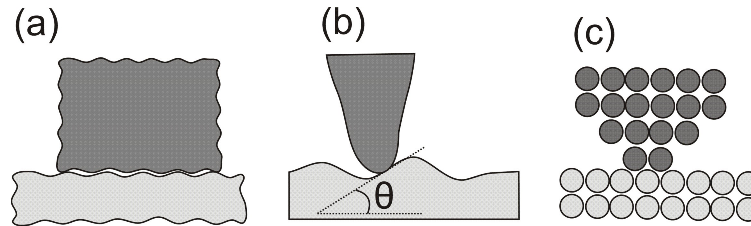

FIGURE 5.1 Schemes of friction at different size scales: (a) Macroscopic friction on a smooth surface due to adhesion and plowing. (b) The nanometer scale and an AFM tip. On a sloped surface the ratchet mechanism gives contribution to the total friction. The angle θ is the local angle between the tip and the sample. (c) The atomic scale and the very endpoint of an AFM tip. Stick-slip friction.

whereas in the collision mechanism the tip suddenly hits the obstacle. Typically, the magnitudes of the material induced effects are independent of the scanning direction, whereas the effects due to the topography depend on the direction of the scanning [6].

Usually during the lateral force measurement with the AFM the wear of the sample is small. Thus the ratchet mechanism gives the main contribution to the local variation of the friction. The effect of the plowing is smaller [7].

The AFM can be used for friction measurements down to the atomic level (figure 5.1 (c)). There the friction comes from the stick-slip motion of the few last atoms on the end of the AFM tip end. Friction corresponds to the energy required for the tip to jump from the one stable equilibrium position into the next one. The periodicity of the friction signal corresponds to the atomic structure of the sample surface [6]. Stick-slip friction can be measured using AFM on an atomically smooth surface such as graphite or mica. During the stick-slip the lateral force signal has peaks with a periodicity corresponding to the atomic distance of the sample. The condition for the stick-slip to occur is that the derivative of the friction force dF_μ/dx is greater than the torsional spring constant of the cantilever [40]. Stick-slip occurs especially between materials that have a matching atomic structure. If the crystal orientations are different, the phenomena can be seen for smaller contact areas [62]. Heimberg et al. imaged a graphite surface with an AFM. They varied the angle between the tungsten tip and the graphite surface and observed a dependency between the measured friction and the orientation. Friction was enhanced with two orientation angles separated by $61^\circ \pm 2^\circ$, which is well in agreement with the 60° periodicity of the graphite. Between the peaks the friction was almost zero due to the super lubricity: because of the mismatch in the crystal orientation only few atoms are touching between the tip and the sample and a joint stick-slip doesn't occur [14].

5.2 Low friction materials

A considerable part of the energy produced today goes to overcome friction and to produce products for replacing worn out parts. Therefore, low friction protective coatings are very much sought for to reduce friction and wear by deposition onto sliding surfaces. One of these coating materials is diamond-like carbon (DLC) . It has excellent tribological properties and can be deposited on many surfaces to prevent corrosion and wear. Typical applications are disks in disk drives, razor blades, metal cutting tools and many components in the car industry. DLC is also used in many space applications because it is lubricant in vacuum, as opposite to the many other materials, which require moisture to become lubricant.

Another example of a low friction material is molybdenum disulfide (MoS_2), which is used as a solid lubricant due to its low friction coefficient. Applications are for example as a component in oil, grease and plastics to decrease friction. It is also used in motors and many vacuum applications. MoS_2 is known to be a solid-film lubricant in vacuum and over large range of temperatures and loads [63].

Superlubricity means that there is no friction between two sliding object. This state can be achieved on a MoS_2 surface, when three criterions are filled. First a molecular layer of MoS_2 must be transferred from the sample (the MoS_2 surface) to the sliding object on top of it. Secondly the MoS_2 planes in the contact interface must reorient to the direction of the sliding. Finally contaminants, such as water, shouldn't be present, since they can modify the shear between the surfaces [39]. Reorientation of the MoS_x was studied experimentally by Zhang et al., who investigated with x-ray diffraction (XRD) , SEM and TEM. They noted that the MoS_x orientates during wear test such that the coefficient of the friction decreases. Simultaneously the wear rate enhances [75]. When the three conditions above are fulfilled, a vanishing friction on a MoS_2 surface can be seen. It vanishes due to the frictional anisotropy, where two crystal lattices are sliding in a small misfit angle (difference in the lattice directions) [39]. This phenomena is called super lubricity and was discussed in the chapter 5.1.

Despite the wide use and investigations on these materials, their properties in the nanoscale domain are not well understood and will certainly be to some extent different. We have studied with AFM the nanotribological properties of MoS_2-Ti.

5.3 Experimental

In this chapter are described the prepration of the hydrophilic and hydrophobic silicon surfaces, the MoS_2-Ti samples, and the CNT material.

Silicon wafer surfaces

The surface of the silicon sample was cleaned with a piranha solution (one ml

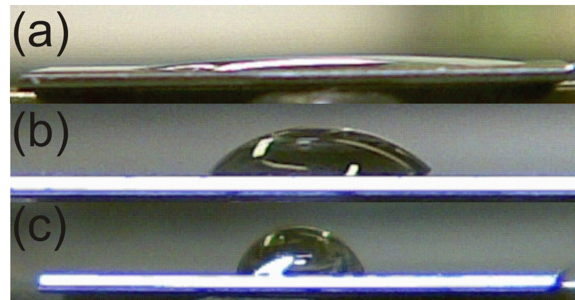

FIGURE 5.2 The figures show how the shape of a water droplet varies with the hydrophilicity of a surface. (a) Hydrophilic silicon after piranha treatment. (b) Unmodified silicon. (c) Hydrophobic silicon after HF treatment.

of hydrogen peroxide (H_2O_2) and three ml of sulfuric acid (H_2S0_4)) . The solution was heated into $90°C$ and the sample was kept there for 15 minutes. The piranha solution cleans the sample by removing the organic material from it. The solution also hydroxylates the sample surface by adding OH groups into it. Thus the treatment makes the sample very hydrophilic.

A hydrophobic silicon surface was prepared by putting the sample into 2 % hydrofluoric acid (HF) for one minute. HF removes the oxide from the sample surface and makes it hydrogen terminated.

The contact angle of the hydrophilic silicon (figure 5.2 (a)) with water is very much decreased from the untreated one (figure 5.2 (b)) after piranha handling. It's approximately $2 - 3°$, determined from figure 5.2 (a). The contact angle for the hydrophobic silicon was approximately $90°$ from figure 5.2 (c).

MoS_2-Ti

The low friction material Molybdenum disulfide titanium (MoS_2-Ti) was received from the Technical Research Centre of Finland (VTT). The sample has a layered structure on high speed steel (HSS) . The top coating of the sample is molybdenum disulphide alloyed with titanium (MoS_2-Ti). The bond coating between the HSS and the MoS_2-Ti is a 100-200 nm thick titanium layer.

Carbon nanotubes

Carbon nanotubes were obtained from two different sources, to increase the range of the diameters of the nanotubes. CNTs fabricated with plasma enhanced chemical vapor deposition (PECVD) are from Koshio et al. Method differs from plasma-assisted catalytic chemical vapor deposition (CCVD) since it doesn't use any catalytic metals or hydrocarbon gases during fabrication [35]. The other nanotube material is from MER corporation and is done by the arc discharge method.

Samples for lateral force measurements across CNT were fabricated by using standard electron beam lithography and vacuum evaporation techniques. These methods were used to fabricate a marker structure on the silicon sample so that it

was possible to locate different nanotubes. The marker structure consists of a square array of 1 micrometer sized crosses 7 micrometers apart, extending for about 50 micrometer. To put nanotubes into the sample with the marker structure they were immersed into 1,2-dichloroethane and spun on the sample surface. Spinning was done by putting the sample to spin at about 3000 RPM and a few drops of CNT-dichloroethane mixture was dropped on the sample. The CNTs were thus randomly deposited.

AFM probes

Contact mode AFM probes were received from Veeco (model DNP-S). The silicon nitride is usually covered with acidic silanol (Si-OH) and basic silazane (Si_2=NH) groups [25], which absorb water. Hence the used unmodified probes can be regarded to be hydrophilic [11].

5.4 Friction on silicon and MoS_2-Ti

Friction was measured on hydrophilic and hydrophobic silicon and MoS_2-Ti surfaces. Measurements were done with the environmental AFM (chapter 3.2) with different normal loads. Lateral force was determined as a difference between the two scanning directions as described in chapter 2.1.2. The lateral vs. normal force plots in ambient conditions for all the three materials (figure 5.3) showed the expected linear behavior.

Measurements of the lateral vs. normal force for the hydrophilic and hydrophobic silicon were done as a function of the setpoint, which determines the normal force of the scanning. On MoS_2-Ti the normal force is plotted as a voltage. Still even for the MoS_2-Ti the friction coefficient can't be determined since without careful calibration, e.g. with a wedge method (chapter 2.2.3), the voltage signals in the horizontal and vertical directions are not comparable. This is due to the higher spring constant of the cantilever for the lateral torsional motion as compared to the bending in the normal direction. The difference is typically two orders of magnitude, e.g. 1 N/m for the normal and 100 N/m for the lateral direction.

5.5 Lateral force across CNT

The carbon nanotube provides an interesting object for friction measurements due to its small size and perfect cylindrical shape. Especially in the round edges of the CNT it's difficult to distinguish between the friction properties of the material and the friction coming from the change in the topography. Lateral forces across MWCNT of different diameters were measured with various AFM tips. In the measurements, peaks on the round edges of the CNT were repeatedly observed (figure 5.4). Lateral

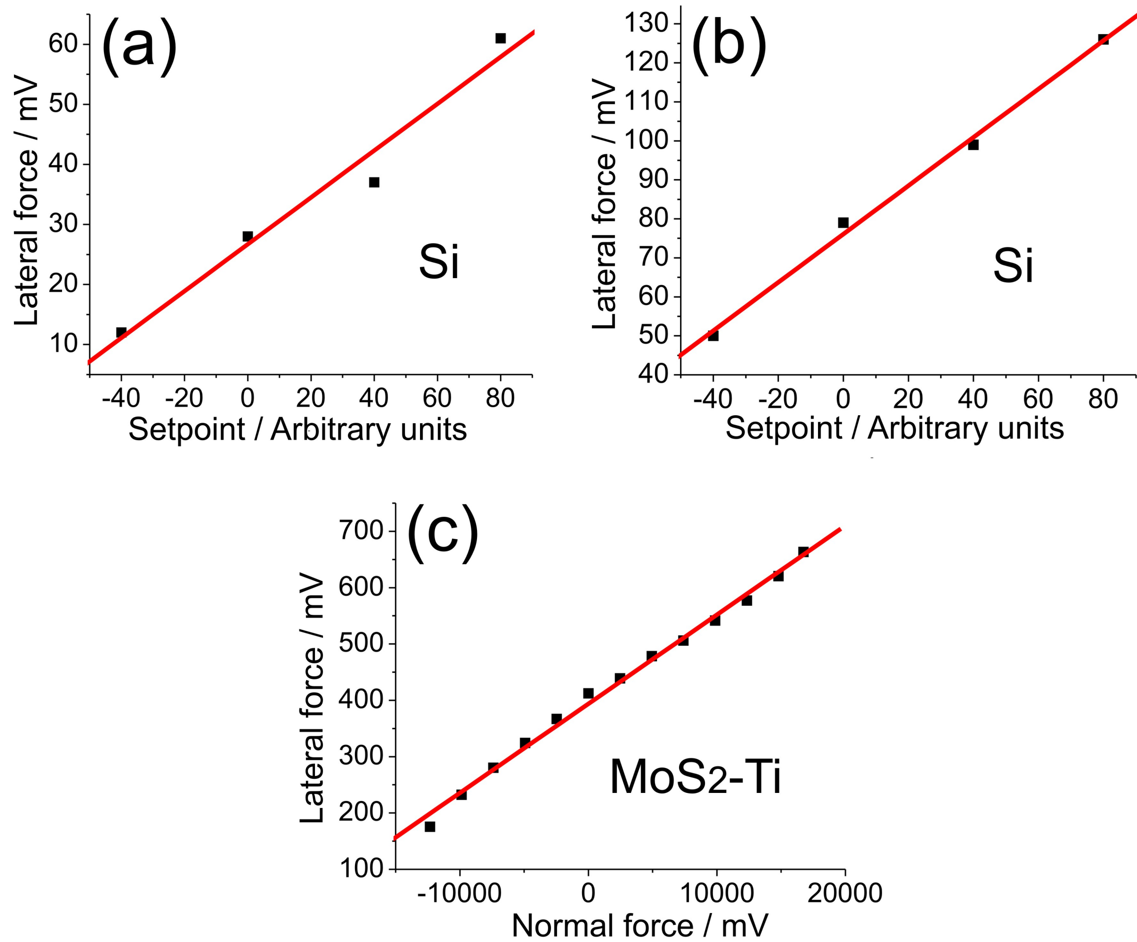

FIGURE 5.3 Measured lateral force for the (a) hydrophilic silicon (b) hydrophobic silicon and (c) MoS_2-Ti in ambient humidity. Scanning length in all the measurements was 400nm.

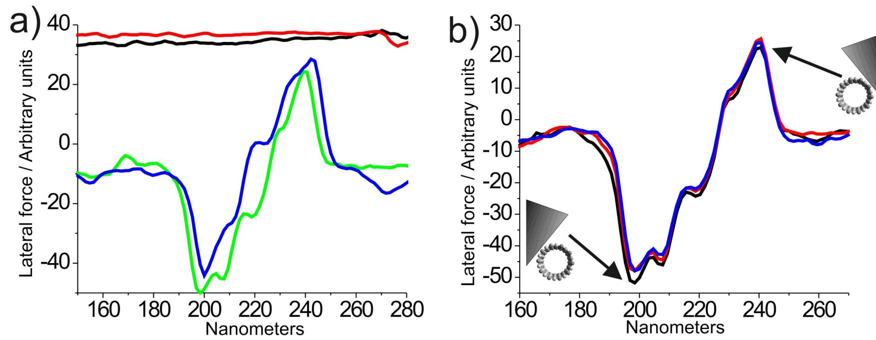

FIGURE 5.4 (a) Measured lateral force across CNT with two different scanning directions. In the black and red curves the cantilever major axis is antiparallel with the CNT. Green and blue curves are taken with the cantilever major axis parallel to the CNT. Latter scanning direction is the typical one in a LF measurement. (b) Three different LF curves to show the reproducibility of the measurement. Also a schematic presentation of the tip slipping on the round edges of the nanotube.

forces during a scan with the cantilever major axis antiparallel to the MWCNT was done to check that there were no contribution of the cross coupling (discussed in the chapter 2.2.3) to the LF data, e.g. due to the misalignment of the photo detector. Both the magnitude and the sign of the peaks were independent of the scanning direction, so they must be due to the slipping of the AFM tip on the round edges of the nanotube.

If the two peaks of the lateral force signal were due to the ratchet mechanism (chapter 5.1), the height of the peaks would depend on the scanning direction. On a scan from left to right an uphill increases the friction, but on a reverse scan (from right to left) the same hill is now a downhill, which decreases the friction. This causes the difference between the LF signals in different scanning direction. Same antisymmetry would be seen also if the signal originated from a collision of the tip into the CNT edge (high peak) and a small relaxation on the other side of the nanotube (small peak).

In figure 5.5 is a schematic presentation of the forces during the AFM tip scanning across the CNT. The total lateral force, including both the friction and the topography effect, is [28]

$$F_L = F_N \cos(\theta)\sin(\theta) + \mu F_N \cos^2(\theta) \tag{5.4}$$

If the friction force is small compared to the LF from the change in topography, the above equation can be simplified into

$$F_L = F_N \cos(\theta)\sin(\theta) \tag{5.5}$$

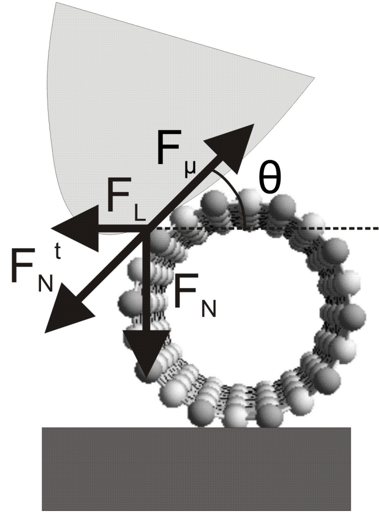

FIGURE 5.5 Forces between the nanotube and the AFM tip during a scan from the right to the left. F_N is the scanning force and F_N^t the tangential component of it. Friction is the F_μ and the lateral force measured by the AFM the F_L. The angle θ is the angle between the sample surface and the CNT/tip contact point.

In the figure 5.6 is given the ratio

$$F_L/F_N = \cos(\theta)\sin(\theta) \tag{5.6}$$

as a blue solid line and the measured lateral force across CNT. Both are plotted as a function of the nanotube radius divided by the tip radius. CNT radius was determined from the topography image and the tip radius by using the formula [22]

$$R_t = \frac{w^2}{16R_{CNT}} \tag{5.7}$$

Lateral force is presented as a difference between the two peaks of the LFM signal on the edges of the CNT.

The calculated ratio between the lateral and normal forces (equation 5.6) approximates well the measured data with small R_{CNT}/R_t, thus confirming the observation that with a dull tip and small CNT the force is more oriented downwards than with a sharp tip and a big nanotube. With higher values of the ratio R_{CNT}/R_t the measured lateral forces deviate significantly from the theoretical plot. It may be explained by irregularities in the shape of the sharper tips.

Also the dependency of the LF on the scanning force was studied. In figure 5.7 is the measured lateral force with different normal forces. At first the scanning force was increased from 6 nN to 130 nN and finally to 250 nN. The repeatability of the measurement was checked by decreasing the force back to approximately the same value as in the first scan. The force of 6 nN was the minimum force, with which the tip was still in contact with the sample. After the measurement a slightly bigger force of 7 nN was required for the imaging to be possible. During imaging the scan-

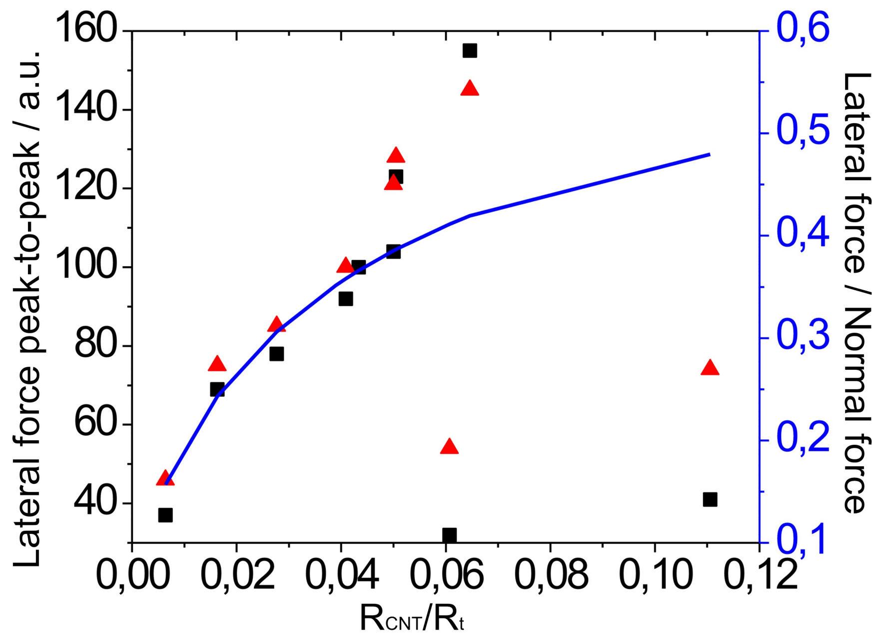

FIGURE 5.6 Measured lateral forces and calculated F_L/F_N (blue solid line) from the equation 5.6 as a function of ratio between the nanotube and tip radiuses. Red triangles represent the data determined from the left-to-right (trace) scan and black rectangles from the right-to-left (retrace) scan.

ning tend to drift slightly, so prior to each image the scanning location was adjusted such that the nanotube was in the middle of the image. Inaccuraties in this setting of the scan location causes the location of the CNT to vary between the different scan images in figure 5.7. During the imaging the CNT showed reversible deformation, which can be seen as a decrease of the CNT diameter when the scanning force was increased. Nanotubes can have this kind of high reversible deformations as described in chapter 4.2.

Location of the CNT varies slightly between the different images due to the drift of the scanner. Prior to each image the scan area was adjusted such that the nanotube was in the middle of the image.

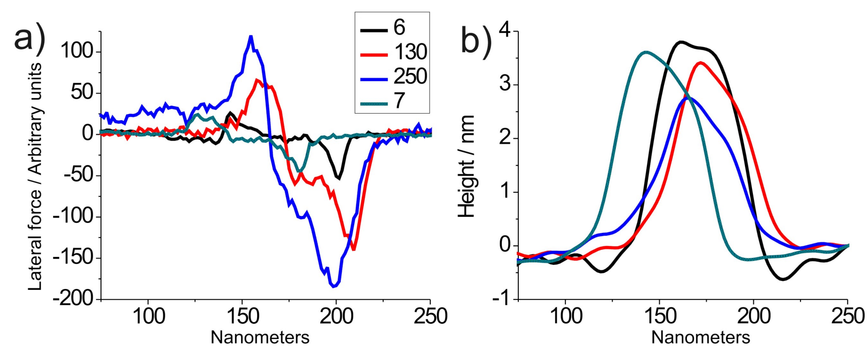

FIGURE 5.7 (a) The measured lateral force with different normal forces of 6, 130, 250 and 7 nanoNewtons. (b) CNT diameter taken simultaneously with the LF measurements.

Chapter 6

Humidity dependence in atomic force microscopy

The water vapor present in air forms a thin layer of water on items exposed to the air. This water layer causes a capillary force, which at the nanometer scale may be a dominant force and must often be taken into account in AFM measurements. In macroscopic systems the friction usually decreases when the humidity increases, since the water layer on surfaces works as a lubricant. On a nanoscale the friction has a quite special behavior, since it's not monotonically decreasing with the humidity. This phenomenon can be seen with the AFM in particular in FZ-curves and in lateral force measurements. It also depends on the hydrophilicity of the sample and the tip. The friction on a hydrophilic material has usually a maximum at a relative humidity of 30 %. Different kind of explanations to this behavior exists, but it's not yet fully understood. Silicon is a suitable material for these studies, since the hydrophilicity of it can be easily modified. In this work, friction dependency on humidity of three different materials was studied by using the AFM in contact mode. All these had different kind of frictional features when studied as a function of the relative humidity.

- The capillary forces in AFM contact mode were studied in hydrophilic and hydrophobic silicon by measuring force-distance curves and friction in a large humidity range.
- The same measurements as above were also done with molybdenum disulfide (MoS_2-Ti) surfaces.

6.1 Laplace theory of capillarity

The Laplace pressure can be used to explain the overpressure inside drops and various curved surfaces of liquids. It also explains the adhesion between an AFM tip

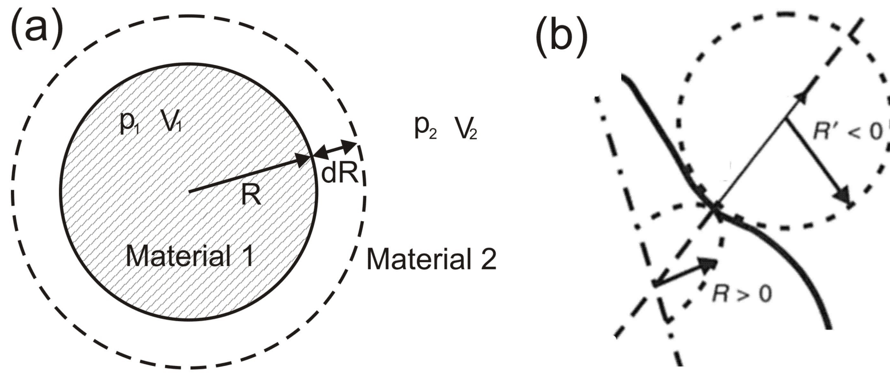

FIGURE 6.1 Drop of liquid (material 1) within gas (material 2). The radius of the droplet R is increased by an amount of dR. The pressures in materials 1 and 2 are p_1 and p_2, respectively. (b) The curvature of a surface C can be calculated with equation 6.6, where R and R' are the radiuses of the curvature of the surface. Radius R is positive (R' negative), since the center of the circle is inside (outside) the object [47].

and a sample surface induced by capillary bridges. There is always a pressure difference between the interfacing curved surfaces of liquids or gases. For example a drop of liquid (material 1) in some gas (material 2) takes a spherical shape to lower its surface energy. If the volume of the sphere is increased by a amount of dR (figure 6.1 (a)), the work done, is

$$dW = -p_1 dV_1 - p_2 dV_2 + \gamma_{12} dA \tag{6.1}$$

where

$$dV_1 = -dV_2 = 4\pi R^2 dR \tag{6.2}$$

is the increase in volume and

$$dA = 8\pi R dR \tag{6.3}$$

in the surface of the sphere. p_1 and p_2 are the pressures and γ_{12} the surface tension between the two materials. γ_{12} is the energy that is required to increase the surface area by one unit. In the mechanical equilibrium the work dW must be zero, so we get from the equation 6.1 that

$$\Delta p = p_1 - p_2 = \frac{2\gamma_{12}}{R} \tag{6.4}$$

The pressure is therefore inversely proportional to the radius of the sphere.

Equation 6.4 can be generalized to any two fluids:

$$\Delta p = \gamma(\frac{1}{R} + \frac{1}{R'}) = \gamma C \tag{6.5}$$

where R and R' are the radii of curvature of the surface (figure 6.1 (b)) and

$$C = \frac{1}{R} + \frac{1}{R'} \tag{6.6}$$

curvature of the surface [47].

The humidity dependent adhesion force gives a contribution to the friction force in AFM measurements. The meniscus is the water pillar from the sample surface to the AFM tip and can form e.g. during FZ-curve sampling (chapter 2.1.3). A schematic image of the meniscus is in figure 6.2. Next an approximation of this force is calculated based on the pressure difference between the meniscus and the surrounding air. The hydrostatic pressure between two fluids is equal to the surface tension γ times the curvature of the surface C (equation 6.5). If thermodynamic equilibrium between the two fluids is assumed, the curvature can be approximated with the Kelvin radius for a three dimensional hemisphere:

$$r_k = \frac{-\gamma V_m}{RTln(RH)} \tag{6.7}$$

In the equation 6.7 V_m is the molar volume of the liquid water ($18.015 \cdot 10^{-6}$ m^3/mol), γ the surface tension (72.75 mNm^{-1} for water at 293 K), R = 8.31 $JK^{-1}mol^{-1}$ the gas constant and T the temperature [5]. For water vapor in air at room temperature the Kelvin radius is [61]

$$r_k = 0.54/ln(RH) \tag{6.8}$$

Now the force between the tip and the sample can be calculated by multiplying the pressure difference with the surface area [61]:

$$F = \Delta p \cdot S_t \tag{6.9}$$

The pressure difference on the surface of the meniscus comes from the equations 6.5 and 6.7, where $C = 1/r_k$:

$$\Delta p = \gamma \cdot C = \frac{RT}{V_m}\ln(RH) \tag{6.10}$$

The surface area is

$$S_t = 2\pi R_t^2(1 - \sin(\omega)) \tag{6.11}$$

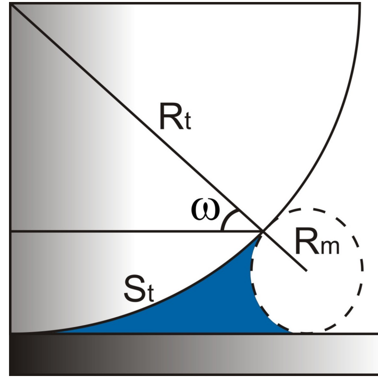

FIGURE 6.2 Meniscus between the AFM tip (radius R_t) and the sample surface. Radius of the meniscus is R_m and the surface area S_t.

where

$$\sin(\omega) = \frac{R_t}{\sqrt{R_t^2 + \frac{4R_t^3 R_m}{(R_t - R_m)^2}}} \tag{6.12}$$

With a RH of 33 %, the radius of the meniscus R_m equals the Kelvin radius $r_k = 0.54/ln(RH) = -0,487\,nm \approx -0.5\,nm$. The pressure difference is $\Delta p \approx 150\,MPa$, the surface area $S_t \approx 6.3 \cdot 10^{-16}\,m^2$ and thus the force $F \approx 94\,nN$.

6.2 The capillary force in AFM

6.2.1 Effect of various parameters

The humidity induced effects in the tip-sample interaction have most directly been recognized in FZ-curve sampling. Other cases include lateral force measurements and tapping mode operation. The capillary force in AFM measurements is found to depend on the scanning force [51], contact time, force and area [18,70], Young modulus of the sample [49], scanning velocity and humidity of the environment [50]. With higher scanning force, the area between an AFM tip and a rough sample increases, thus allowing more small water bridges to form. The friction depends on the amount and size of these menisci, thus increasing with increasing scanning force [51]. Friction is inversely proportional to the Young modulus of the sample, since softer samples have a bigger contact area with the tip, which increases friction [49]. When the scanning is slow, more menisci can form, which again increases the friction [50]. In chapters 6.2.2 - 6.2.6 the capillary effect on hydrophilic and hydrophobic silicon and molybdenum disulfide will be discussed.

6.2.2 Capillary effects on tapping mode

During tapping mode the interaction with the sample affects the amplitude and phase shift of the cantilever oscillation. Zitzler et al. have done amplitude-phase-distance (APD) curves on hydrophilic and hydrophobic silicon. They varied the free amplitude A_0 and the humidity between the measurements. The APD curve is analogous to a FZ-curve in contact mode. The difference is that during APD curve sampling the cantilever is oscillating as in tapping mode and the collected data during the curve sampling are the amplitude and phase shift of the cantilever oscillations. Zitzler et al. found that with low oscillation amplitude the amplitude decreases linearly and the phase shift shows a continuous increase. This positive phase shift means an attractive tip-sample interaction. With high amplitude the phase shift first increases, but after the critical distance suddenly becomes negative due to the repulsive interaction. In the same location there is also a discontinuity in the amplitude data. The measurement was repeated with different amplitudes and humidities for hydrophilic and hydrophobic samples and the critical amplitude A_c with which there was a jump to the repulsive regime, was determined. The critical amplitude A_c had an increase on the hydrophilic sample but not on the hydrophobic sample. The hysteresis during the APD curve comes from the formation and breakage of a water meniscus between the tip and the sample [78].

6.2.3 Reported capillary effects in hydrophilic materials

For hydrophilic silicon the friction has a maximum at relative humidity of about 30 %. The phenomenon is not fully understood, but different kind of explanations are given. One is that the friction first increases as the meniscus forms between the objects (e.g. AFM tip and the sample surface) and then decreases as the radius of the meniscus increases. This can be understood from the fact that the Laplace pressure ΔP is inversely proportional to the radius of the meniscus, as discussed in chapter 6.1.

Another explanation assumes that during FZ-curve sampling, the capillary force depends on the volume of the meniscus. Willett et al. have found that pull-off distance is approximately proportional to the cubic root of the volume [68] which was experimentally verified by Sirghi et al. [61]. Monte Carlo simulations have shown that during FZ-curve sampling for a wide meniscus the volume can increase even if the distance between the AFM tip and the sample surface increases, thus giving a maximum at some RH [32].

The adhesion force between a SiO_2 sample and a hydrophilic silicon nitride AFM tip was measured with FZ-curve sampling by Chen et al. They saw a maximum on the force with the RH between 45 and 75 %. Similar measurement on hydrophobic methyl (CH_3) showed no dependency on the humidity. The sample had a 100 nm layer of gold on top of a silicon chip. The gold was treated with CH_3

terminated with a 1-octadecanethiol. Chen et al. performed also lateral force measurements on a sample with SiO_2 stripes on a CH_3 surface. The SiO_2 showed higher friction due to the bigger adhesion force. The contrast between the two different materials followed qualitatively the adhesion force measurements showing lowest contrast at $RH = 10\,\%$, highest at $RH = 53\,\%$ and intermediate at $RH = 90\,\%$ [11].

Force-distance measurements by Xiao et al. on a SiO_2 surface showed a maximum at RH = 65 %. They also calculated the tip-sample capillary force based on the pressure difference between the meniscus and the surrounding air (chapter 6.1) and the surface tension. The calculation showed a dependency of the capillary force on the tip shape: the maximum of the adhesion force shifts up in RH as the tip gets duller. However, they weren't able to see it experimentally [70].

Asay et al. explain the maximum of the capillary force by formation of icelike water even at room temperature. They have studied the structure of water condensates on a silicon oxide surface by attenuated-total-reflection infrared spectroscopy (ATR-IR) [4]. An ice-like structure can occur because water is able to form a tetrahedral coordinated network [3]. The ice structure of water has also been verified by AFM, since Jinesh et al. observed stick-slip motion with a periodicity close to the lattice constant of the hexagonal ice [33].

In the ATR-IR method, the infrared beam travels through the silicon sample and reflects at the surface. The natural logarithm of the inverse reflectance is then plotted as a function of the wave number. From this spectrum the different configurations and thicknesses of the water layer can be determined. Asay et al. found three different regions on the water adsorption (figure 6.3). On region A, the ice-like structure starts to grow on top of the silicon oxide surface. On the next region the amount of the ice-like water saturates and liquid water begins to grow. Finally, on region C the ice-like water has saturated and more liquid water grows on top of the ice-like water [3].

Greiner et al. studied friction with a heated probe and noticed that friction on hydrophilic silicon (piranha treatment) depends on the temperature of the tip. In ambient condition the friction was increased due to the thermally assisted formation of the capillary bridge between the tip and the sample. In a dry nitrogen environment the friction was decreased as a function of the probe temperature because of the thermally assisted sliding [23].

6.2.4 Reported capillary effects in hydrophobic materials

The adhesion force on a hydrophobic OTE/SiO_2 sample with a Si_3N_4 AFM tip was measured by Xiao et al.. The measurement was done with FZ-curve sampling in a humidity range of 5-98 %, but no dependency of the tip-sample adhesion force on RH was found [70].

The adhesion force between two silica spheres (average diameter $1.7\,\mu m$) were studied by Fuji et al.. Unmodified silica is hydrophilic, but hexamethyldisilazan

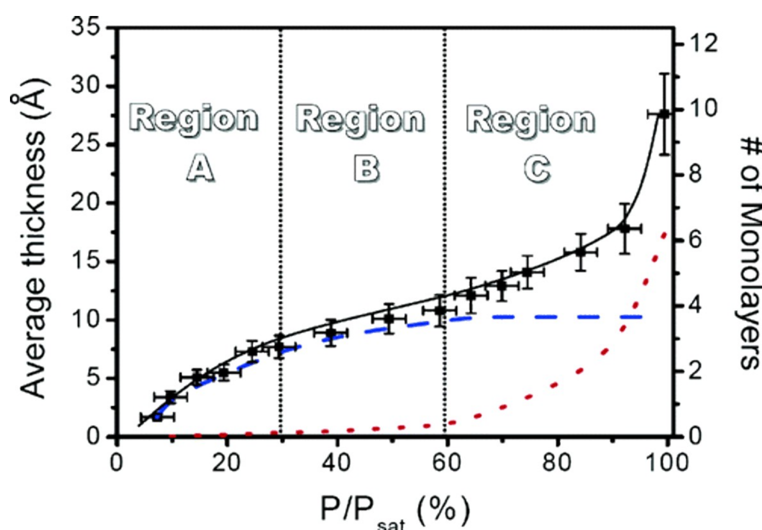

FIGURE 6.3 Three different regions of water adsorption on the silicon oxide surface. Blue dotted line indicates the thickness of the ice-like water, red dotted line the amount of the liquid water and the black solid line the total water thickness [3].

(HMDS) was used to partly cover the spheres with trimethylsilyl (TMS) . The measurement was done by attaching one silica sphere to the AFM tip and another one to a flat silicon plate. The adhesion force was determined from FZ-curve sampling in the relative humidity ranging from 40 % to 90 %. With the hydrophilically modified and the unmodified silica spheres the adhesion force was approximately constant up to a RH of 70 %. With even higher humidity the force started to increase. A slightly modified, but still hydrophilic tip-sample pair showed similar behavior, but now the increase started with a RH of 90 %. This sudden increase in the adhesion force is due to the capillary condensation (formation of the water meniscus). For the less hydrophilic tip and sample the contact angles of the material with water are smaller, which produces smaller Kelvin radius and thus shifts the capillary condensation into a higher RH. With the hydrophobic silica spheres a gradual increase didn't occur, so apparently there is no capillary condensation between them [20].

The formation of the meniscus between the silica spheres was already studied in the earlier work of Fuji et al.. They used a volumetric method to determine the adsorption of HMDS modified spheres. In the volumetric apparatus the gas is put into a recirculation loop and it's pressure and temperature are measured. These measurements give the initial number of moles of the gas in the loop. Then the gas is allowed to contact the adsorbent and after the equilibrium the pressure and the temperature are measured again. The number of moles remaining in the gas phase can then be calculated. The amount of the adsorbed gas can then be gained as a difference between the initial and the gas phase values [34].

Using the method described above, Fuji et al. measured the adsorption of silica spheres with different hydrophilicity. The absorbance of the unmodified sphere was higher than the absorbance of the sphere with 39 % (slightly hydrophilic) and 42

% (hydrophobic) coverage of the TMS. A sphere with a 39 % coverage had a rapid increase as a function of RH, up close to 100 %. Whereas the sphere with a 42 % coverage had only 65 % of the monolayer adsorption, with RH = 100 %. The difference of the adsorbed water in low humidity can be explained by the amount of silanol on the sample (addition of the TMS decreases the amount of silanol). Since the water is absorbed by the silanol, the higher amount of silanol means more water adsorbed. Fuji et al. determined also the adsorption of the water molecules per silanol. With the hydrophilic sample the adsorption decreases with decreasing amount of silanol, but the amount of water molecules per silanol is the same as for the unmodified sample. For the hydrophobic sample, the TMS groups are shielding the silanols and the amount of adsorbed water molecules per silanol is lower. In the unmodified sample, as the RH increases a multilayer of water is formed. This is also the case with the hydrophilic sample (39 % coverage), despite the increase in distance between the water islands (due to the TMS) before the formation of the multilayer. This capillary condensation causes the increase of the adhesion force with RH of 70 %. On a hydrophobic sample (42 % coverage of TMS) this kind of capillary condensation doesn't occur, since even with a RH = 100 %, only 65 % is adsorbed of the volume that would be required for a monolayer of water to form. Thus the lack of capillary condensation on a hydrophobic sample results in that there is no increase in the adhesion force with increasing RH [19].

Fukunishi et al. studied the adhesion force between a hydrophobic sample (octadecyltrichlorosilane (OTS) treated silica, OTS/Silica) and a glass bead or AFM tip. The adhesion force was constant as a function of RH with the sphere-sample configuration. In turn, the AFM tip with a OTS/Silica had a decreasing adhesion force with increasing humidity. Fukunishi et al. concluded that there is no increase in the adhesion force, because the hydrophobic sample doesn't form a capillary neck with the tip or the sphere, as suggested by Fuji et al. (refs. [19,20]). They also calculated, based on the Laplace theory, under which conditions the capillary neck forms between a spherical particle and a flat surface. Equation 6.5 and a modified 6.7 (also the water contact angles of the two materials were taken into account) were used to calculate, whether the meniscus can occur on a hydrophobic sample (contact angle $110°$). The meniscus can't form when RH is below 35 %, even with a strongly hydrophilic sphere (contact angle $0°$). If the contact angle of the sphere is above $70°$, the meniscus isn't formed even with RH = 100 %. So the meniscus can't form if the both materials (tip and the sample) are hydrophobic, but forms with high RH if at least one of the materials is hydrophilic [21].

6.2.5 Reported capillary effects in MoS_2

Friction of molybdenum disulfide (MoS_2) measured with a ball on a flat tribotester and an AFM has a dependency on the humidity of the environment [36]. Peterson

et al. measured friction with a tribotester and observed an increase in friction as a function of the relative humidity. Also the wear of the slider was higher at the high humidity [46].

Zhao et al. measured the friction on a MoS_2 surface with a silicon nitride (Si_3N_4) and a MoS_2 terminated tip. The friction coefficient, determined as a slope from the lateral force vs. normal force plots, was measured at different humidities. It showed an increase as a function of the humidity with both tips. The only difference between the tips was that with Si_3N_4 the increase was smooth whereas with a MoS_2 terminated tip a sharp increase in friction occurred with RH between 40 % and 50 % [77].

The friction on $MoS_2 - Al$ showed a similar increase with increasing humidity as the pure MoS_2. Nainaparampil et al. measured the friction from RH of 0 % to the 40 %. At first the friction coefficient increases with RH = 0-25 % and is then approximately constant with RH at 25 %-40 %. In the measurements a ball on a flat tribotester was used [42].

Schumacher et al. measured the humidity dependence of the friction on MoS_2 single layers using the AFM. They had two different kinds of supporting materials for the layers: mica and aluminum oxide Al_2O_3. Measurements were performed in the humidity range of 5 %-90 %. On both supporting materials the friction coefficient of the MoS_2 was almost constant during the whole measurement range [58].

Zhang et al. have measured the friction and wear of MoS_x coating with a corundum sphere in contact with the surface. Measurements were performed at different humidities and velocities with two different kind of MoS_x samples: random and basal oriented. They noticed that for the random oriented sample the coefficient of friction and the wear rate increased significantly with increasing humidity. With basal oriented MoS_x the increase in friction and wear was much smaller. Measurements with different velocities showed that the friction was higher, when the measurement was done with a higher sliding speed [76]. Also opposite studies, where the friction has decreased as a function of rising velocity, exists. In these works the reason is that the adsorbed water is removed from the surface due to the frictional heating [36].

6.2.6 Summary of previous work on the capillary force in AFM and our contribution

As a summary of the chapters 6.2.4 and 6.2.5, the capillary force on a hydrophilic material has a maximum, or increases strongly, at some RH (typically $\approx 30\,\%$), while in hydrophobic material there is not much of dependence on the humidity conditions. Molybdenum disulfide has a lowest capillary force with low RH and increases with increasing humidity.

Many theories exist to explain in hydrophilic materials the maximum in the capillary force as a function of the RH. One quite widely used theory explains the

increase as due to the formation of the capillary meniscus and, as the RH is raised further, the following decrease to be caused by the lowering of the Laplace pressure inside the meniscus, which in turn is caused by the increase in its radius. The fact that there is no dependency of the capillary force on RH on a hydrophobic sample can simply be attributed to the lack of tip-sample capillary meniscus. The increase in friction of MoS_2 can be explained by water modifying the easy shear (possibly superlubricity) of the two surfaces.

Adhesion force measurements with varying humidity are typically done by FZ-curve sampling, as described in chapter 6.2. Measurements on the lateral force as a function of RH has been done more rarely. Of combinations of these two we are aware of only one, which measured the tip-sample force between the Si_3N_4 tip and the SiO_2/CH_3 sample. More detailed description of that measurement is in chapter 6.2.3 (ref. [11]). In contrast to this study, here we have measured the lateral force by scanning on a smooth hydrophilic silicon surface and the LF is determined as a difference between the two scanning directions, while in ref. [11] only a qualitative change in the contrast of the two areas (SiO_2 and CH_3) were observed. Any numerical values of the LF weren't presented. Therefore, the study on the effect of humidity on AFM operation which is presented below, is to our knowledge the first one which directly compares the humidity dependence as seen with force-distance measurements and with lateral force measurements.

6.3 Experimental

We have in this work studied experimentally the dependence of friction and normal force on the humidity when using AFM in contact mode. Lateral force and FZ measurements with varying relative humidity were done together for hydrophilic and hydrophobic silicon, while for MoS_2-Ti only lateral force measurements were done. From the FZ-curves the pull-off distance, which is comparable to the adhesion force, was determined as described in chapter 2.1.3. An example of a single FZ-measurement in this work was shown in chapter 3, figure 3.5. All the materials had different kind of frictional features when studied as a function of the relative humidity. The measurements were done with the environmental-AFM of chapter 3.2. The results of all the three materials are from a typical measurement representing a considerable number of similar measurements.

The set of humidity dependent measurements was done as follows: Humidity was first increased to the maximum value, typically 60 % by introducing water vapor into the chamber, after which it was gradually reduced to the lowest achievable value of a few percent. At the maximum humidity value, the environment was left to stabilize for half an hour after which the first LF and FZ-curve measurements were performed. For the stepwise reduction of the humidity, a quick drying was done by circulating air through the drying silica pellets and after stabilization of

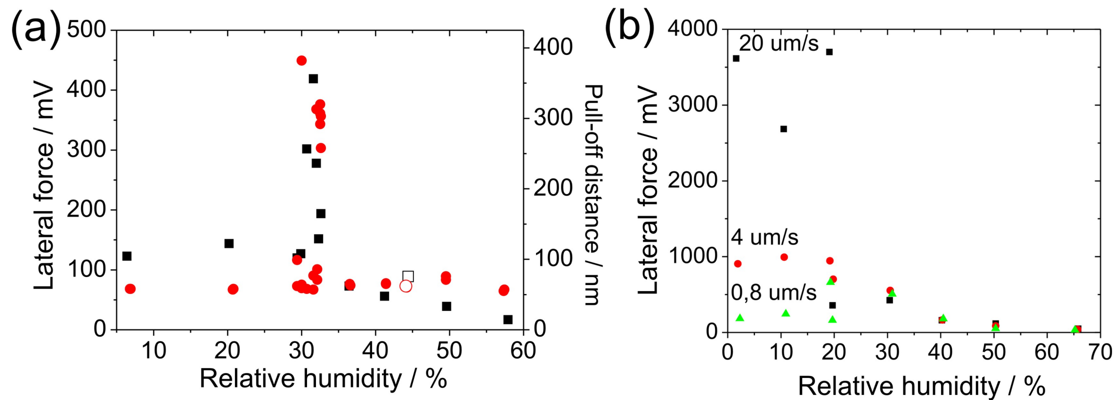

FIGURE 6.4 (a) Lateral force (black squares) and pull-off distance (red circles) as a function of the RH for hydrophilic silicon. The measurements were done by reducing the RH from 60 % to 5 %. The open symbols indicate a measurement repeated at $RH \approx 45\%$ after the main measurement series. (b) Lateral force measured as a function of the RH with three different scanning speeds. The lowest speed is roughly the same as the one used in (a)

the air (approx. 15 minutes), a new measurement was performed. Measurements were repeated down to a RH of a few percents. To check the repeatability of the measurements, after the whole humidity range was gone through, the LF and FZ-curve measurement were repeated with RH of 45 % (open symbols). The humidity was measured before and after each measurement. It tends to drift slightly upwards during the measurement, probably because the humidity conditions weren't fully stabilized. At maximum this drift was 0.5 % in RH.

6.4 Measurements

Hydrophilic silicon

The scanning area in the LF measurements on silicon was $400 \cdot 400\ nm^2$. Both the simultaneously measured friction and the pull-off distance on hydrophilic silicon as a function of humidity are shown in figure 6.4 (a). As expected based on the discussion in chapter 6.2, both show a very strong increase with RH above 30 %. The shape and the location of both peaks are very similar.

The maximum force between the tip and the sample at RH = 33 % was calculated with the Laplace theory presented in chapter 6.1. The result was about 94 nN. The maximum pull-off distance in the FZ measurements was about 300 nm (figure 6.4), which gives an adhesion force of $0.24\ N/m \cdot 300\ nm = 72\ nN$. This is close to the theoretical value of 94 nN from the Laplace theory. In the calculation above the spring constant of the cantilever of 0.24 N/m was the value given by the manufacturer (Bruker). It's an average value and can vary between 0.12 and 0.48 N/m. The pull-off distance is almost constant around the peak, with values clearly below

hundred nanometers and a minimum distance of $\approx 60\ nm$. So the adhesion force increases from $0.24\ N/m \cdot 60\ nm \approx 14\ nN$ to 72 nN, due to the change in humidity. The increase is more than 400 %. It's close to the value of Chen et al., who also found a 400 % increase in the adhesion force from $\approx 13\,nN$ into $\approx 65\,nN$ [11]. On the contrary to this work, Chen et al. found only a quite small decrease of the adhesion force with high humidity (from 65 nN to $\approx 50\,nN$).

However, the velocity dependence of the friction force was also tested and the friction at low humidities showed a strong increase with increasing scanning speed, as shown in figure 6.4 (b). In the figure, the lowest velocity is (roughly) the same as in (a), and this data is also essentially reproduced. At higher velocities, however, the behavior changes drastically. Moreover, this behavior is qualitatively opposite to the one reported by Riedo et al. [50] on different materials though. Their results were explained as due to the kinetics of the capillary condensation, since with a lower scanning speed more menisci can form between the tip and the sample. Here we note that the measurement of the capillary adhesion via the pull-off distance in the FZ-curve is a static case of capillarity compared to the LF measurement with a sweeping tip. We can conclude that the dynamics of the observed effects play a significant role, but we did not at this stage pursue this topic further.

Hydrophobic silicon

The adhesion force between the tip and the sample on a hydrophobic sample (figure 5.2 (c)) showed no dependence on the humidity, when measured with FZ-curve sampling, as shown in figure 6.5. The measurement range was from 0 % to 75 % in relative humidity. The constant adhesion force is in agreement with the previous studies described in chapter 6.2.4, where the pull-off distance vs. RH was constant or even decreased with increasing humidity. Friction measurements on a hydrophobic sample showed a minimum at a relative humidity of about 40 % (figure 6.5), which is opposite behavior compared to hydrophilic silicon, which had a maximum at a RH above 30 %. Also, the magnitudes of the lateral forces, over the whole range of measured RH, are about an order of magnitude less than the peak value in hydrophilic silicon. Unmodified silicon nitride probe is hydrophilic, as discussed in chapter 5.3 (ref. [11]).

According to Fukunishi et al. (ref. [21]), the water meniscus can, in such a case with a hydrophilic tip over a hydrophobic surface, still form if the RH gets close to 100 %. The friction on hydrophobic silicon was approximately independent of the scanning speed. The dynamics of the tip-sample interaction must be different between the FZ measurements and the friction measurements, due to the difference in the measured forces. Previously the capillary force is found to depend on the tip-sample contact time (ref. [18]), so the tip being much longer time in contact with the

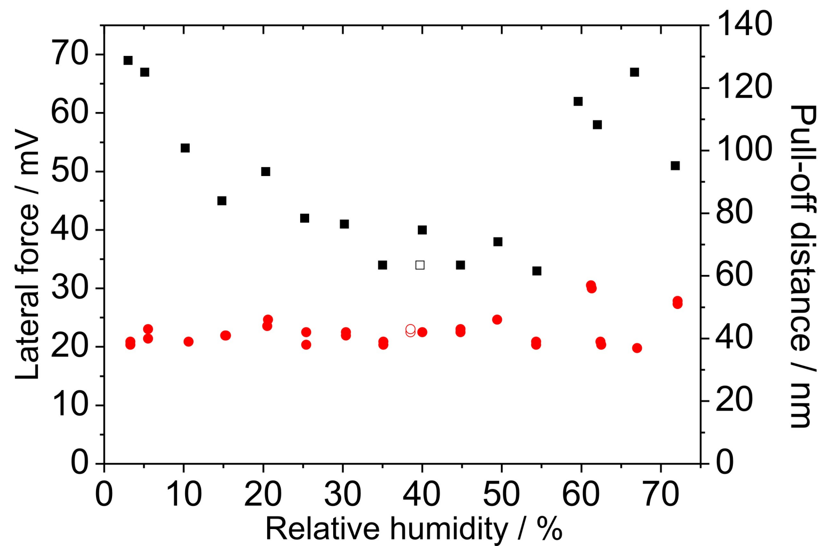

FIGURE 6.5 Lateral force (black squares) and pull-off distance (red circles) as a function of the RH for hydrophobic silicon. The measurements were done by reducing the RH from 75 % downwards. The open symbols indicate a measurement repeated at $RH \approx 40\,\%$ after the main measurement series.

sample in LF measurement compared to the FZ-curve sampling may be the reason for the difference in the data.

Molybdenum disulfide

Friction on the MoS_2-Ti surface was measured at varying humidity. The scanning area was $2 \cdot 2\ \mu m^2$ and the speed was varied by changing the frequency of the scanning tip. A frequency of 1Hz produced a scanning speed of $4\ \mu m/s$ ($2\ \mu m$ back and forth), and 0.2 Hz and 5 Hz the speeds $0.8\ \mu m/s$ and $20\ \mu m/s$, respectively. In another study (data not shown) the change in speed was done by keeping the frequency constant and the scan size was changed. The results were similar compared to this study.

The friction increased with increasing RH and scanning speed as can be seen from figure 6.6. It is in agreement with the previous studies discussed in chapter 6.2.5. There it was suggested that the water would modify the sliding condition of the two surfaces and thus increase the friction.

We may conclude that capillarity is a rich source of effects for the tip-sample interaction. The observed effects are a sum of the contributions from many factors among which are substrate and tip materials (especially their hydrophilicity) and tip velocity. Capillarity can not be ignored in nanotribological studies.

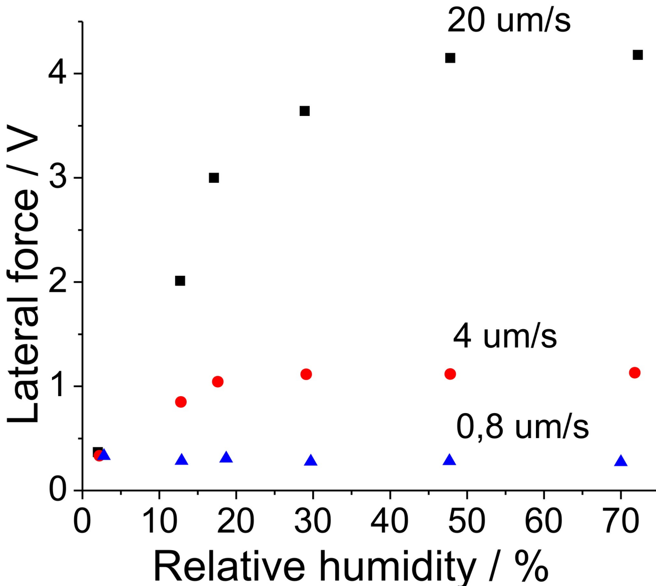

FIGURE 6.6 Measured lateral force as a function of relative humidity for MoS_2-Ti with different scanning speeds. Humidity was first measured with a RH of 72 % and then decreased as was descriped in the chapter 6.4.

Chapter 7

AFM tip shape estimation

The AFM can image samples with sub nanometer resolution in height direction, but the resolution can be significantly reduced in the horizontal direction due to the finite size of the tip. This finite size of the tip, at the scale where it images objects on a surface, is conventionally estimated with the assumption that the tip apex is semispherical in shape. The size can then be estimated with a single number, the tip radius of this semisphere. In this chapter we explore the effects of the finite size and the shape of currently used tips in AFM imaging.

- A method is described with which the real shape of AFM tips was estimated from images taken on objects of known shape, such as MWCNT's and microfabricated steps. In particular, we are interested in how the apex of the tip at the nanometer scale deviates from the semispherical form with which it is commonly approximated. [Publication A.IV].

7.1 Convolution

The effect of the tip shape on the AFM images is called convolution and the process used to remove this effect deconvolution. Due to the convolution convex features appear wider (e.g. particle on a surface) and concave structures (e.g. holes) narrower in the images [15].

Convolution occurs always in the AFM images, but there are some special cases, when this phenomenon is remarkably enhanced. Such cases are e.g. contaminated or broken tips. Especially biological or other soft samples tend to contaminate the tip. Sometimes the tip can break so that multiple tips form to the end of the probe. This is called multiple tip effect and can also be due to the contamination, if a particle attaches near the tip apex [15]. One example of the convolution due to the contamination of the tip is given in figure 7.1. There an image of a MWCNT is tripled (figure 7.1 (a) and (b)) due to a contamination particle attached to the AFM

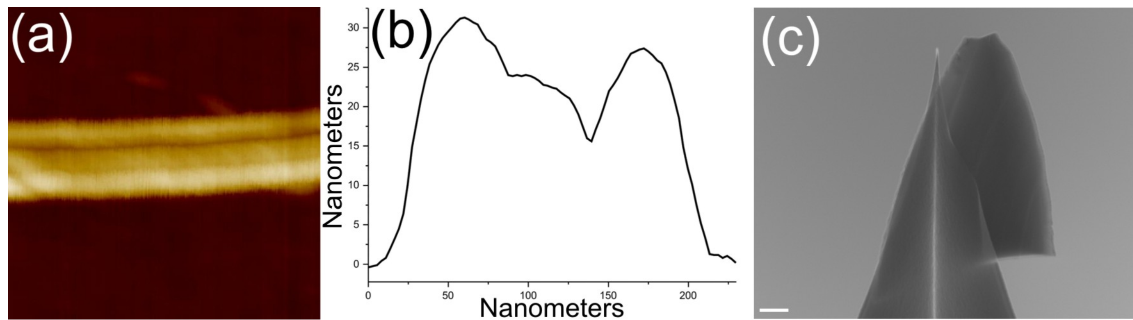

FIGURE 7.1 (a) CNT imaged with a contaminated tip. A clear triple tip effect can be seen. Imaged area is $700 \cdot 700\ nm^2$ (b) Cross-section of the same nanotube, taken from a one scanning. (c) Contaminated tip with a contamination particle attached to the tip apex, causing the artifact in the image. Scale bar is 100 nanometers.

tip (figure 7.1 (c)). The tip is otherwise very sharp, but the contamination particle widens the image of the nanotube remarkably.

When imaging samples with high aspect ratio, the etched side of the probe, above the tip apex, can also give a contribution to the image. This occurs especially with silicon nitride contact mode tips, which have typically very wide opening angles (up to $40°$). If the side of the probe affects too much the imaging, probes with smaller opening angles should be used. Tapping mode tips have usually lower angles, down to $15°$. In more precise measurement, special high aspect ratio probes (opening angle less than $3°$) can be used [15].

If the tip shape is approximated as a sphere or as a cone, the convolution effect can easily be removed from the images. However, the shape of the AFM probe is never in any simple geometrical shape, so more elaborate methods are usually required [15].

One way to determine the actual shape of the AFM tip is to image it with TEM or SEM. A problem with these methods is that only a one dimensional image is gained. So, in order to achieve a three dimensional image, the tip must be imaged multiple times and rotated between the images. Also the low resolution of the images and contamination or damage of the tip during imaging can be a problem [15].

Another method uses AFM itself to determine the shape of the tip. The imaged object can be e.g. sharp pikes, the shape of which can be ignored, if they are much sharper than the tip. Also samples with known shape can be used as a characterizer. Such can be e.g. different kind of nanoparticles, like CNT's [15, 67].

Tip shape can also be calculated with so called blind reconstruction, which doesn't require any additional sample for the deconvolution process [15]. In the reconstruction the tip shape is approximated in each data point of the AFM image and the final tip shape taken as a minimum of these curves. The process is repeated iteratively until it converges [65].

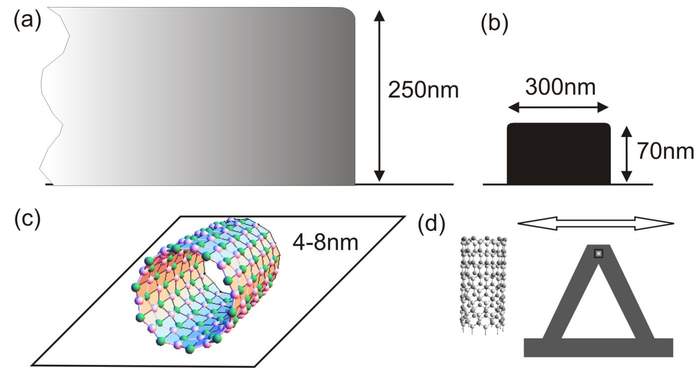

FIGURE 7.2 Three structures used for a tip shape approximation: (a) 250 nm height silicon nitride membrane, (b) Gold line of a 70 nm height and (c) multiwall carbon nanotube. In (d) is depicted the scanning direction during the tip shape approximation. The direction was the same also with the SiN membrane and the Au-line.

7.1.1 Experimental

The shape of the AFM tip was determined by scanning with it across three different objects of different heights: a silicon nitride membrane of 250 nm height, a 70 nm high line of metal (titanium in our case) and a MWCNT (see figure 7.2 (a)-(c)). The last object, the MWCNT, has in principle a cross section (which is spherical) which is known with an Ångström level accuracy, and can thus enable very precise tip shape determination. Scanning was done with the cantilever major axis parallel and the fast scan axis perpendicular to the structure as in the figure 7.2 (d). Only with the nanotube was numerical data processing employed to obtain quantitative tip shape profiles. With the microfabricated objects, the obtained data was used for more qualitative insight on the tip shape issue.

The numerical approximation procedure used the Villarrubias tip shape approximation algorithm. In the Villarrubias erosion algorithm, the tip shape is calculated by using the known shape of the nanotube (approximated as a cylinder with straight edges, as in figure 7.3) and the measured topographical data. Cavities of the nanotube don't need to be taken into account since the AFM tip can't reach them even if it were infinitely sharp. Firstly, the measured topography of the nanotube is reflected (dash lines in the figure 7.4). Then the shape of the tip is approximated with the same resolution as the recorded image. The principle of the algorithm is such that the tip is positioned above the sample and then lowered until it touches the sample surface in one or more points. From this point one proportion of the tip approximation is gained. The method is repeated in each point of the image (only five points shown in figure 7.4) and the final tip shape is gained as an erosion of these proportions (blue dash line). By this method an upper bound of the tip shape is gained. It doesn't necessarily give the real shape of the tip, but is, with this kind of model, the best possible maximum approximation for the tip shape [66].

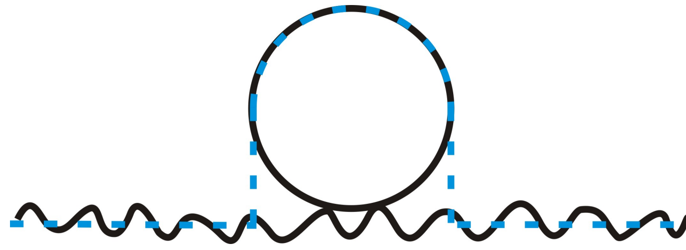

FIGURE 7.3 Carbon nanotube approximated as a cylinder.

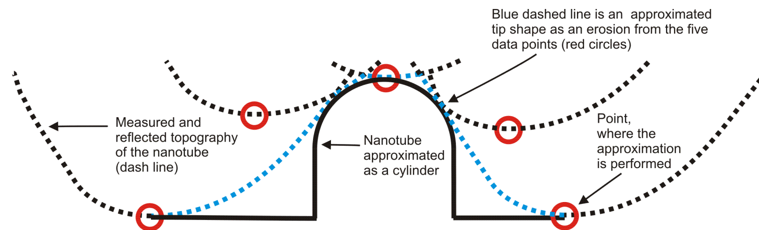

FIGURE 7.4 Schematic illustration of the used algorithm for the tip shape approximation.

7.1.2 Tip shape estimation with microfabricated steps

Tips can be approximated at most on a distance that is the height of the imaged object. With CNTs this distance was less than six nanometers in the measurements described below in chapter 7.1.3. To extend the approximated distance, objects with higher vertical dimensions were used. Such objects were a titaniumum line and a silicon nitride membrane. In figure 7.5 (a) is a topography of the SiN membrane together with the actual shape of it (red dotted line) and a theoretical profile, if the tip were infinitely sharp with an etching angle of $17.5°$. The actual shape of the membrane is almost vertical, forming a square with the sample surface. Also the edge of the membrane is only slightly rounded, as can be seen from the SEM image (figure 7.6).

In figures 7.5 (c) and (e) are the measured profiles of the Ti-line and in (b) and (d) the SEM images of the tips used for the imaging. The tips were imaged with the SEM after the AFM maesurement. In profile (e) there is a clear antisymmetry, which clearly corresponds to the antisymmetry visible in the SEM image in (d)).

7.1.3 Tip shape estimation with carbon nanotubes

Four different numerically calculated tip shapes from the image data from scans across CNT's in tapping mode are shown in figure 7.7. Included with these are lines that illustrate the spherical approximation. In the figures 7.7 (b) and (d), two different sphere approximations are done, where the red curve follows the very end of the AFM tip and the green curve as an average of the whole approximated distance of the tip. From the figure it can be seen that the spherical approximation rarely fol-

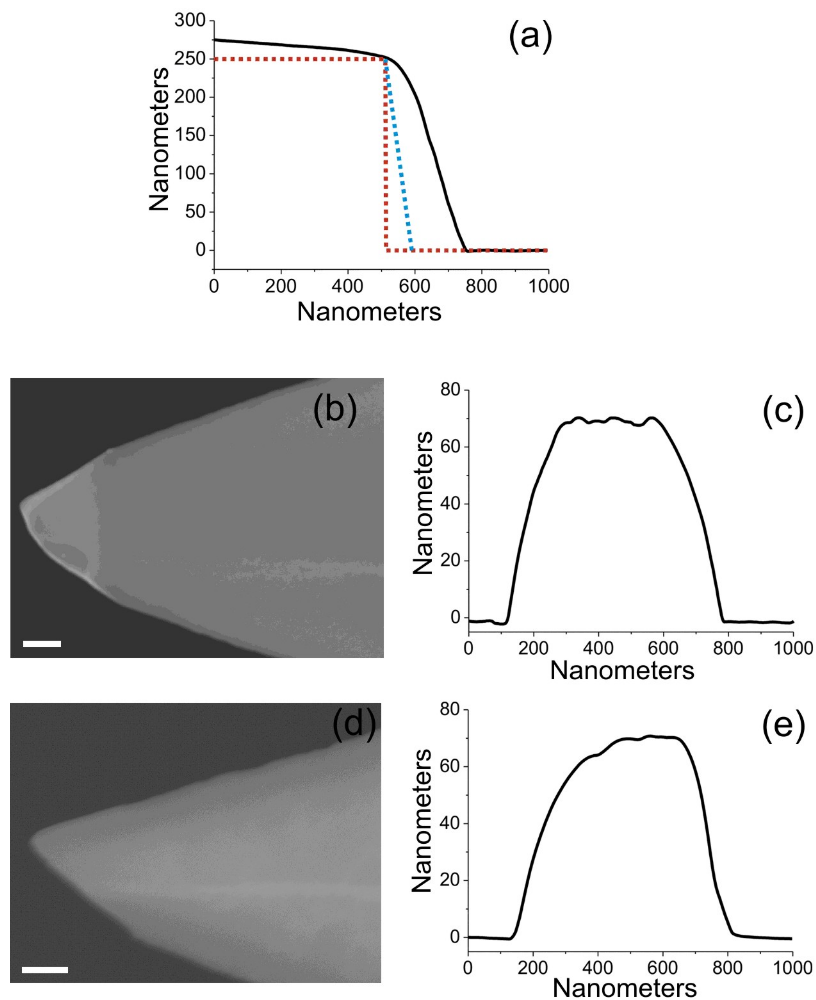

FIGURE 7.5 (a) Black solid line is the measured profile and red dotted line the actual shape of the SiN membrane. Blue dotted line is the profile, that would be measured with a infinitely sharp tip with a $17.5°$ etch angle. In (c) and (e) are the measured profiles across the aluminum line (units in nanometers) and in the (b) and (d) the corresponding tip imaged taken with a SEM. Scale bars in both images are 100 nm.

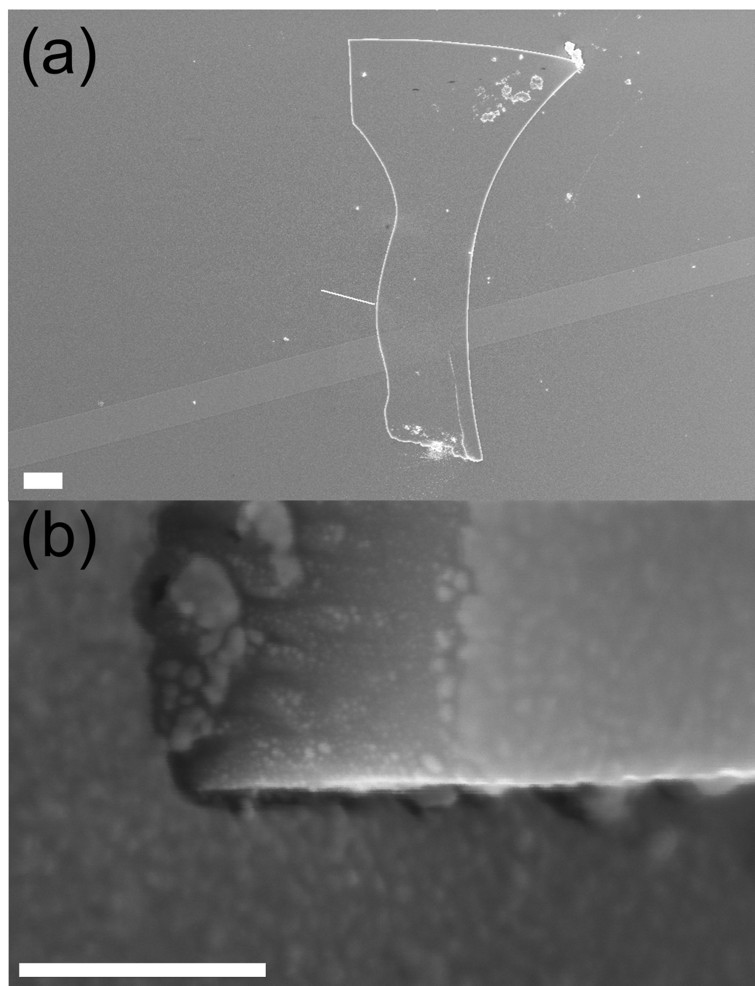

FIGURE 7.6 (a) SiN membrane imaged with SEM from the top. Scale bar is 10 μm. (b) The same membrane imaged with SEM from the side showing the straight edge of the membrane and the small curvature of the edge. Scale bar is 200 nm.

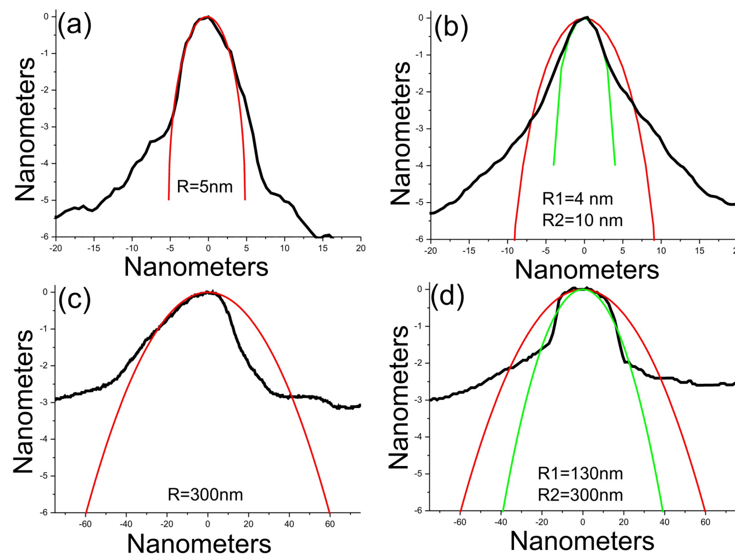

FIGURE 7.7 Various tip shapes approximated as a sphere with radius R. Topography data is from a scan across CNT.

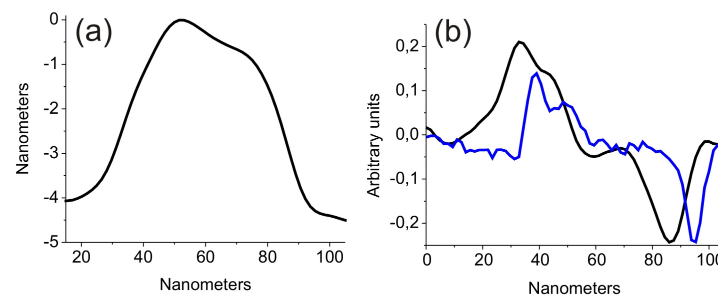

FIGURE 7.8 (a) Calculated tip shape from a contact mode scan across CNT. (b) Derivative of the topography data (black curve) and lateral force during imaging (blue curve).

lows the actual tip shape. The difference can be due to the antisymmetric tip as in the figure 7.7 (c) or due to the difference in the shape of the tip apex compared to the rest of the tip (figure 7.7 (b) and (d)).

Tip shape approximations were done also in contact mode. Simultaneously with the imaging the lateral force was collected. In figure 7.8 (a) is an approximated tip shape from a scan across nanotube. The tip is clearly antisymmetric, which can be seen also from the derivative of the topography data (the black curve in figure 7.8 (b)). The same antisymmetry is visible in the lateral force data (blue curve in the figure 7.8 (b)). The higher peak in LF occurs in the CNT edge where the slope of the tip is higher. This result is in agreement with the previous studies of the lateral force across CNT's with different nanotubes and tip radiuses in chapter 5.5. There it was concluded that the peak-to-peak distance of the LF increases as a function of the slope between the nanotube and the tip.

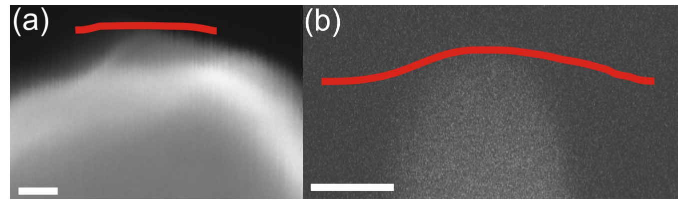

FIGURE 7.9 Calculated tip shape (red curve) from a scan across CNT with a SEM image of the same tip. Scale bar 10 nm.

The calculated profiles from the contact mode data (red curves in the figure 7.9 superimposed to the SEM images) were compared to the SEM images of the same tips. A coincidence between the two exists, but a good matching between the two is difficult to obtain. The difference is mainly due to the limited accuracy of the SEM with this kind of objects in the nanometer scale. Nevertheless, a combination of SEM (or TEM) imaging with the AFM method outlined in this chapter seems very promising for producing tip shape estimates for such imaging tasks where an accurate knowledge of the tip profile is useful or necessary.

Chapter 8

Conclusions

The surrounding air can significantly affect both the AFM images and the force measurements. Especially humidity and air pressure are affecting the AFM measurements. In order to perform AFM studies in controlled conditions, an AFM with environmental control was built. In the project a commercial AFM was placed inside an aluminum chamber. Some small modifications had to be done e.g. to the optics and the sample stage. Inside the chamber humidity and pressure can be controlled. Imaging can also be done in various non-corrosive gases like helium or nitrogen.

Carbon nanotubes have many remarkable mechanical and electrical properties. Elasticity of MWCNTs were measured by spinning nanotubes on a sample with microfabricated gold lines. Nanotubes were randomly oriented and some of them were partly suspended on the edge of the Au-line. The distance d, which the CNT is suspended before it touches the silicon surface, was measured with the AFM in tapping mode. The measurement was repeated with three different line heights of 16, 32 and 45 nanometers. CNT diameters were between 3 and 13 nm. The distances d were in agreement with a theoretical model, where the balance between the elastic restoring force and the van der Waals attraction force between the nanotube and the sample was taken into account.

Friction measurements on three different kinds of samples were performed with the env-AFM. The samples were hydrophilic and hydrophobic silicon and the low friction material MoS_2-Ti. First the friction was measured with different normal loads and the expected linear behavior was found on all the samples. Measurement was done also in different humidity. Hydrophilic silicon showed a maximum in friction and in pull-off distance of the FZ-curves with the RH = 30 %. On a hydrophobic silicon the pull-off distance was constant during the whole RH measurement range from below 10 % to the approximately 75 %. Friction had a minimum on the $RH \approx 40\,\%$. On the MoS_2-Ti the friction increased with increasing RH.

Shapes of the AFM tips were approximated with the MWCNTs and micro fabricated steps. Nanotubes were used to approximate the very end of the AFM tip. When the approximation is done with the CNTs the approximated height is limited by the small size of the nanotubes (typically less than ten nanometers). To overcome

this issue, micro fabricated steps with heights of 70 nm and 250 nm were used. After the tip shape approximation the tips were imaged with a SEM and results compared. On a scan across 70 nm line antisymmetry on topography data was seen. With the SEM imaging it was confirmed that the antisymmetry was due to the antisymmetric AFM tip.

Bibliography

[1] *diDimension V instruction manual* (Veeco, 2006).

[2] ALBRECHT, T., AKAMINE, S., CARVER, T., AND QUATE, C., *Microfabrication of cantilever styli for the atomic force microscope*. JOURNAL OF VACUUM SCIENCE & TECHNOLOGY A-VACUUM SURFACES AND FILMS **8** (1990) 3386–3396.

[3] ASAY, D. AND KIM, S., *Evolution of the adsorbed water layer structure on silicon oxide at room temperature*. JOURNAL OF PHYSICAL CHEMISTRY B **109** (2005) 16760–16763.

[4] ASAY, D. AND KIM, S., *Effects of adsorbed water layer structure on adhesion force of silicon oxide nanoasperity contact in humid ambient*. JOURNAL OF CHEMICAL PHYSICS **124** (2006) 174712.

[5] ATKINS, P. AND DE PAULA, J., *physical chemistry, 7th edition* (Oxford, 2002).

[6] BHUSHAN, B., *Principles and applications of tribology* (JOHN WILEY and SONS, INC., 1999).

[7] BHUSHAN, B., *Nanotribology and Nanomechanics An Introduction Second Edition* (Springer, 2008).

[8] BINNIG, G., QUATE, C., AND GERBER, C., *Atomic force microscope*. PHYSICAL REVIEW LETTERS **56** (1986) 930–933.

[9] BINNIG, G. AND ROHRER, H., *Scanning tunneling microscopy*. HELVETICA PHYSICA ACTA **55** (1982) 726–735.

[10] BURT, D. P., DOBSON, P. S., DONALDSON, L., AND WEAVER, J. M. R., *A simple method for high yield fabrication of sharp silicon tips*. MICROELECTRONIC ENGINEERING **85** (2008) 625–630.

[11] CHEN, L., GU, X., FASOLKA, M. J., MARTIN, J. W., AND NGUYEN, T., *Effects of Humidity and Sample Surface Free Energy on AFM Probe-Sample Interactions and Lateral Force Microscopy Image Contrast*. LANGMUIR **25** (2009) 3494–3503.

[12] CLEVELAND, J., MANNE, S., BOCEK, D., AND HANSMA, P., *A nondestructive method for determining the spring constant of cantilevers for scanning force microscopy*. REVIEW OF SCIENTIFIC INSTRUMENTS **64** (1993) 403–405.

[13] CLIFFORD, C. A. AND SEAH, M. P., *Improved methods and uncertainty analysis in the calibration of the spring constant of an atomic force microscope cantilever using static experimental methods*. MEASUREMENT SCIENCE & TECHNOLOGY **20** (2009) 125501.

[14] DIENWIEBEL, M., VERHOEVEN, G., PRADEEP, N., FRENKEN, J., HEIMBERG, J., AND ZANDBERGEN, H., *Superlubricity of graphite*. PHYSICAL REVIEW LETTERS **92** (2004) 126101.

[15] EATON, P. AND WEST, P., *Atomic force microscopy* (Oxford University Press, 2010).

[16] ENDO, M., *Grow carbon-fibers in the vapor-phase*. CHEMTECH **18** (1988) 568–576.

[17] FALVO, M., CLARY, G., TAYLOR, R., CHI, V., BROOKS, F., WASHBURN, S., AND SUPERFINE, R., *Bending and buckling of carbon nanotubes under large strain*. NATURE **389** (1997) 582–584.

[18] FERREIRA, O. D. S., GELINCK, E., DE GRAAF, D., AND FISCHER, H., *Adhesion experiments using an AFM-Parameters of influence*. APPLIED SURFACE SCIENCE **257** (2010) 48–55.

[19] FUJI, M., IWATA, H., TAKEI, T., WATANABE, T., AND CHIKAZAWA, M., *The change in the water vapor affinity of fine silica particles loaded with trimethylsilyl groups*. ADVANCED POWDER TECHNOLOGY **8** (1997) 325–334.

[20] FUJI, M., MACHIDA, K., TAKEI, T., WATANABE, T., AND CHIKAZAWA, M., *Effect of wettability on adhesion force between silica particles evaluated by atomic force microscopy measurement as a function of relative humidity*. LANGMUIR **15** (1999) 4584–4589.

[21] FUKUNISHI, A. AND MORI, Y., *Adhesion force between particles and substrate in a humid atmosphere studied by atomic force microscopy*. ADVANCED POWDER TECHNOLOGY **17** (2006) 567–580.

[22] GRAVELAND-BIKKER, J. AND DE KRUIF, C., *Self-assembly of hydrolysed alpha-lactalbumin into nanotubes*. FEBS JOURNAL **272** (2005) 550.

[23] GREINER, C., FELTS, J. R., DAI, Z., KING, W. P., AND CARPICK, R. W., *Local Nanoscale Heating Modulates Single-Asperity Friction*. NANO LETTERS **10** (2010) 4640–4645.

[24] GUO, T., NIKOLAEV, P., THESS, A., COLBERT, D., AND SMALLEY, R., *Catalytic growth of single-walled nanotubes by laser vaporization*. CHEMICAL PHYSICS LETTERS **243** (1995) 49–54.

[25] HACKLEY, V. AND MALGHAN, S., *The surface-chemistry of silicon-nitride powder in the presence of dissolved ions*. JOURNAL OF MATERIALS SCIENCE **29** (1994) 4420–4430.

[26] HAMIDINEZHAD, H., WAHAB, Y., AND OTHAMAN, Z., *Ultra-sharp pointed tip Si nanowires produced by very high frequency plasma enhanced chemical vapor deposition via VLS mechanism*. Journal of Materials Science (2011) 1–5. 10.1007/s10853-011-5435-6, URL `http://dx.doi.org/10.1007/s10853-011-5435-6`.

[27] HERTEL, T., WALKUP, R., AND AVOURIS, P., *Deformation of carbon nanotubes by surface van der Waals forces*. PHYSICAL REVIEW B **58** (1998) 13870–13873.

[28] HONG, D. K., HAN, S. A., PARK, J. H., TAN, S. H., LEE, N., AND SEO, Y., *Frictional force detection from lateral force microscopic image using a Si grating*. COLLOIDS AND SURFACES A-PHYSICOCHEMICAL AND ENGINEERING ASPECTS **313** (2008) 567–570.

[29] HUTTER, J. AND BECHHOEFER, J., *Calibration of atomic-force microscope tips*. REVIEW OF SCIENTIFIC INSTRUMENTS **64** (1993) 1868–1873.

[30] IIJIMA, S., *Helical microtubules of graphitic carbon*. NATURE **354** (1991) 56–58.

[31] JAI, C., AIME, J. P., MARIOLLE, D., BOISGARD, R., AND BERTIN, F., *Wetting an oscillating nanoneedle to image an air-liquid interface at the nanometer scale: Dynamical behavior of a nanomeniscus*. NANO LETTERS **6** (2006) 2554–2560.

[32] JANG, J., YANG, M., AND SCHATZ, G., *Microscopic origin of the humidity dependence of the adhesion force in atomic force microscopy*. JOURNAL OF CHEMICAL PHYSICS **126** (2007) 174705.

[33] JINESH, K. AND FRENKEN, J., *Capillary condensation in atomic scale friction: How water acts like a glue*. PHYSICAL REVIEW LETTERS **96** (2006) 166103.

[34] KAUL, B., *Modern version of volumetric apparatus for measuring gas solid equilibrium data*. INDUSTRIAL & ENGINEERING CHEMISTRY RESEARCH **26** (1987) 928–933.

[35] KOSHIO, A., YUDASAKA, M., AND IIJIMA, S., *Metal-free production of high-quality multi-wall carbon nanotubes, in which the innermost nanotubes have a diameter of 0.4 nm*. CHEMICAL PHYSICS LETTERS **356** (2002) 595–600.

[36] LANCASTER, J., *A review of the influence of environmental humidity and water on friction, lubrication and wear*. TRIBOLOGY INTERNATIONAL **23** (1990) 371–389.

[37] LI, Q., KIM, K., AND RYDBERG, A., *Lateral force calibration of an atomic force microscope with a diamagnetic levitation spring system*. REVIEW OF SCIENTIFIC INSTRUMENTS **77** (2006) 065105.

[38] MARCUS, R., RAVI, T., GMITTER, T., CHIN, K., LIU, D., ORVIS, W., CIARLO, D., HUNT, C., AND TRUJILLO, J., *Formation of silicon tips with less-than-1 nm radius*. APPLIED PHYSICS LETTERS **56** (1990) 236–238.

[39] MARTIN, J., DONNET, C., LEMOGNE, T., AND EPICIER, T., *Superlubricity of molybdenum-disulfide*. PHYSICAL REVIEW B **48** (1993) 10583–10586.

[40] MATHEW MATE, C., *Tribology on the Small Scale* (Oxford University Press, 2008).

[41] MEYER, E., HUG, H. J., AND BENNEWITZ, R., *Scanning Probe Microscopy* (Springer-Verlag, 2004).

[42] NAINAPARAMPIL, J., PHANI, A., KRZANOWSKI, J., AND ZABINSKI, J., *Pulsed laser-ablated MoS2-Al films: friction and wear in humid conditions*. SURFACE & COATINGS TECHNOLOGY **187** (2004) 326–335.

[43] NEUMEISTER, J. AND DUCKER, W., *Lateral, normal, and longitudinal spring constant of atomic-force microscopy cantilevers*. REVIEW OF SCIENTIFIC INSTRUMENTS **65** (1994) 2527–2531.

[44] OGLETREE, D., CARPICK, R., AND SALMERON, M., *Calibration of frictional forces in atomic force microscopy*. REVIEW OF SCIENTIFIC INSTRUMENTS **67** (1996) 3298–3306.

[45] PALACI, I., FEDRIGO, S., BRUNE, H., KLINKE, C., CHEN, M., AND RIEDO, E., *Radial elasticity of multiwalled carbon nanotubes*. PHYSICAL REVIEW LETTERS **94** (2005) 175502.

[46] PETERSON, M. AND JOHNSON, R., *Friction and wear investigation of molybdenum disulfide: I - effect of moisture*. National Advisory Committee for Aeronautics **Technical Note 3055** (1953).

[47] PIERRE-GILLES, D. G., FRANCOISE, B.-W., AND DAVID, Q., *Capillarity and Wetting Phenomena: Drops, Bubbles, Pearls, Waves* (Springer, 2004).

[48] RAVI, T., MARCUS, R., AND LIU, D., *Oxidation sharpening of silicon tips*. JOURNAL OF VACUUM SCIENCE & TECHNOLOGY B **9** (1991) 2733–2737.

[49] RIEDO, E. AND BRUNE, H., *Young modulus dependence of nanoscopic friction coefficient in hard coatings*. APPLIED PHYSICS LETTERS **83** (2003) 1986–1988.

[50] RIEDO, E., LEVY, F., AND BRUNE, H., *Kinetics of capillary condensation in nanoscopic siding friction*. PHYSICAL REVIEW LETTERS **88** (2002) 185505.

[51] RIEDO, E., PALLACI, I., BORAGNO, C., AND BRUNE, H., *The 2/3 power law dependence of capillary force on normal load in nanoscopic friction*. JOURNAL OF PHYSICAL CHEMISTRY B **108** (2004) 5324–5328.

[52] RUOFF, R., QIAN, D., AND LIU, W., *Mechanical properties of carbon nanotubes: theoretical predictions and experimental measurements*. COMPTES RENDUS PHYSIQUE **4** (2003) 993–1008.

[53] SADER, J., *Parallel beam approximation for V-shaped atomic-force microscope cantilevers*. REVIEW OF SCIENTIFIC INSTRUMENTS **66** (1995) 4583–4587.

[54] SADER, J., CHON, J., AND MULVANEY, P., *Calibration of rectangular atomic force microscope cantilevers*. REVIEW OF SCIENTIFIC INSTRUMENTS **70** (1999) 3967–3969.

[55] SADER, J., LARSON, I., MULVANEY, P., AND WHITE, L., *Method for the calibration of atomic-force microscope cantilevers*. REVIEW OF SCIENTIFIC INSTRUMENTS **66** (1995) 3789–3798.

[56] SAITO, P., DRESSELHAUS, G., AND DRESSELHAUS, M. S., *Physical properties of carbon nanotubes* (Imperial College Press, 1999).

[57] SCHMITZ, I., SCHREINER, M., FRIEDBACHER, G., AND GRASSERBAUER, M., *Phase imaging as an extension to tapping mode AFM for the identification of material properties on humidity-sensitive surfaces*. APPLIED SURFACE SCIENCE **115** (1997) 190–198.

[58] SCHUMACHER, A., KRUSE, N., PRINS, R., MEYER, E., LUTHI, R., HOWALD, L., GUNTHERODT, H., AND SCANDELLA, L., *Influence of humidity on friction measurements of supported MoS2 single layers*. JOURNAL OF VACUUM SCIENCE & TECHNOLOGY B **14** (1996) 1264–1267. 8th International Conference on Scanning Tunneling Microscopy and Related Methods (STM 95), SNOWMASS, CO, JUL 25-29, 1995.

[59] SHEIKO, S., MOLLER, M., REUVEKAMP, E., AND ZANDBERGEN, H., *Calibration and evaluation of scanning-force-microscopy probes*. PHYSICAL REVIEW B **48** (1993) 5675–5678.

[60] SHEN, W., JIANG, B., HAN, B., AND XIE, S., *Investigation of the radial compression of carbon nanotubes with a scanning probe microscope*. PHYSICAL REVIEW LETTERS **84** (2000) 3634–3637.

[61] SIRGHI, L., SZOSZKIEWICZ, R., AND RIEDO, E., *Volume of a nanoscale water bridge*. LANGMUIR **22** (2006) 1093–1098.

[62] SORENSEN, M., JACOBSEN, K., AND STOLTZE, P., *Simulations of atomic-scale sliding friction*. PHYSICAL REVIEW B **53** (1996) 2101–2113.

[63] STEWART, T. AND FLEISCHAUER, P., *Chemistry of sputtered molybdenum-disulfide films*. INORGANIC CHEMISTRY **21** (1982) 2426–2431.

[64] VARENBERG, M., ETSION, I., AND HALPERIN, G., *An improved wedge calibration method for lateral force in atomic force microscopy*. REVIEW OF SCIENTIFIC INSTRUMENTS **74** (2003) 3362–3367.

[65] VILLARRUBIA, J., *Scanned probe microscope tip characterization without calibrated tip characterizers*. JOURNAL OF VACUUM SCIENCE & TECHNOLOGY B **14** (1996) 1518–1521.

[66] VILLARRUBIA, J., *Algorithms for scanned probe microscope image simulation, surface reconstruction, and tip estimation*. JOURNAL OF RESEARCH OF THE NATIONAL INSTITUTE OF STANDARDS AND TECHNOLOGY **102** (1997) 425–454.

[67] WANG, Y. AND CHEN, X., *Carbon nanotubes: A promising standard for quantitative evaluation of AFM tip apex geometry*. ULTRAMICROSCOPY **107** (2007) 293–298.

[68] WILLETT, C., ADAMS, M., JOHNSON, S., AND SEVILLE, J., *Capillary bridges between two spherical bodies*. LANGMUIR **16** (2000) 9396–9405.

[69] WONG, E., SHEEHAN, P., AND LIEBER, C., *Nanobeam mechanics: Elasticity, strength, and toughness of nanorods and nanotubes*. SCIENCE **277** (1997) 1971–1975.

[70] XIAO, X. AND QIAN, L., *Investigation of humidity-dependent capillary force*. LANGMUIR **16** (2000) 8153–8158.

[71] YAN, S., XU, Y., YANG, J., WANG, H., JIN, Z., AND WANG, Y., *A novel fabrication method of silicon nano-needles using MEMS TMAH etching techniques*. NANOTECHNOLOGY **22** (2011).

[72] YOUNG, H. AND FREEDMAN, R., *University Physics with modern physics, 10th edition* (Addison-Wesley, 2000).

[73] YU, M., KOWALEWSKI, T., AND RUOFF, R., *Investigation of the radial deformability of individual carbon nanotubes under controlled indentation force*. PHYSICAL REVIEW LETTERS **85** (2000) 1456–1459.

[74] YU, M., LOURIE, O., DYER, M., MOLONI, K., KELLY, T., AND RUOFF, R., *Strength and breaking mechanism of multiwalled carbon nanotubes under tensile load*. SCIENCE **287** (2000) 637–640.

[75] ZHANG, X., LAUWERENS, W., HE, J., AND CELIS, J., *Reorientation of randomly oriented MoSx coatings during fretting wear tests*. TRIBOLOGY LETTERS **17** (2004) 607–612.

[76] ZHANG, X., LAUWERENS, W., STALS, L., HE, J., AND CELIS, J., *Fretting wear rate of sulphur deficient MoSx coatings based on dissipated energy*. JOURNAL OF MATERIALS RESEARCH **16** (2001) 3567–3574.

[77] ZHAO, X. AND PERRY, S. S., *The Role of Water in Modifying Friction within MoS(2) Sliding Interfaces*. ACS APPLIED MATERIALS & INTERFACES **2** (2010) 1444–1448.

[78] ZITZLER, L., HERMINGHAUS, S., AND MUGELE, F., *Capillary forces in tapping mode atomic force microscopy*. PHYSICAL REVIEW B **66** (2002) 155436.